Quantifying Precipitation Efficiency and Drivers of Excessive Precipitation in Post-Landfall Hurricane Harvey

NOAH S. BRAUER

Advanced Radar Research Center, School of Meteorology, University of Oklahoma, Norman, Oklahoma

JEFFREY B. BASARA

School of Meteorology, and School of Civil Engineering and Environmental Science, University of Oklahoma, Norman, Oklahoma

CAMERON R. HOMEYER

School of Meteorology, University of Oklahoma, Norman, Oklahoma

GREG M. MCFARQUHAR

School of Meteorology, University of Oklahoma, and Cooperative Institute for Mesoscale Meteorological Studies, Norman, Oklahoma

PIERRE E. KIRSTETTER

Advanced Radar Research Center, School of Meteorology, University of Oklahoma, and NOAA National Severe Storms Laboratory, Norman, Oklahoma

(Manuscript received 19 August 2019, in final form 21 January 2020)

ABSTRACT

Hurricane Harvey produced unprecedented widespread rainfall amounts over 1000 mm in portions of southeast Texas, including Houston, from 26 to 31 August 2017. The highly efficient and prolonged warm rain processes associated with Harvey played a key role in the catastrophic flooding that occurred throughout the region. Precipitation efficiency (PE) is widely referred to in the scientific literature when discussing excessive precipitation events that lead to catastrophic flash flooding, but has yet to be explored or quantified in tropical cyclones coincident with polarimetric radar observations. With the introduction of dual-polarization radar to the NEXRAD WSR-88D network, polarimetric radar variables such as Z_H, Z_{DR}, and K_{DP} can be used to gain insight into the precipitation processes that contribute to enhanced PE. It was found that 6-h mean values of Z_H between 35 and 45 dBZ, Z_{DR} between 1 and 1.5 dB, and K_{DP} greater than 1° km^{-1} were collocated with the regions of PE greater than 100% between 27 and 29 August. Additionally, supercell thunderstorms embedded in the outer bands of Harvey were identified via 3–6 km Multi-Radar Multi-Senor (MRMS) rotation tracks and were collocated with swaths of enhanced positive Z_H, Z_{DR}, and K_{DP}. A polarimetric rainfall relationship estimates that 1-h mean rainfall rates in these supercells were as high as 85 mm h^{-1} and made a significant contribution to the excessive precipitation event that occurred over the region.

1. Introduction

Excessive precipitation events that result in flooding are the second-deadliest meteorological hazard after excessive heat (Ashley and Ashley 2008). Although flooding tends to be particularly detrimental to life and property in developing countries, in recent years developed countries such as the United States have had impactful events when flooding is collocated with large population centers. The overall severity of the flooding depends not only on the rainfall rate and the duration of the heavy precipitation, but also land use of the region, topography, and antecedent soil moisture prior to the event.

Landfalling tropical cyclones that have formed in the Atlantic basin are responsible for an estimated 500 000

Corresponding author: Noah S. Brauer, nbrauer@ou.edu

DOI: 10.1175/JHM-D-19-0192.1

fatalities since 1492, including 25 000 deaths in the United States (e.g., Rappaport and Fernandez-Partagas 1997; Rappaport 2000, 2014). While storm surge poses a major threat to coastal areas, excessive precipitation events associated with tropical cyclones that occur hundreds of miles inland have been responsible for thousands of fatalities in North America. For example, Tropical Storm Allison produced catastrophic flooding in southeast Texas in 2001, with a total rainfall accumulation of 940 mm observed at the Port of Houston and a resulting 24 deaths (National Weather Service 2001).

Radar observations from the operational WSR-88D network are useful in cases of landfalling tropical cyclones as they provide observations at a high temporal resolution (e.g., Medlin et al. 2007; Didlake and Kumjian 2018). Such observations allow for the identification of mesoscale features contained within the spiral rainbands and eyewall. The processes occurring in these features can ultimately enhance rainfall rates at the surface. Traditionally, the equivalent radar reflectivity factor at horizontal polarization (Z_H) has been used to estimate the surface rainfall rate using a power law relationship. Such relationships between Z_H and rainfall rate (R) are typically derived empirically (e.g., Rosenfeld et al. 1993; Crosson et al. 1996), referred to generally as Z–R relationships, and depend on the drop size distribution and other factors such as the presence of partial beam filling and path attenuation (e.g., Rosenfeld et al. 1993; Ryzhkov et al. 2005b). Thus, the use of Z–R relationships may be useful for determining the threat of flash flooding in warning operations, but may become problematic when the drop size distribution varies between the convective and the stratiform components of tropical cyclones, or between tropical and extratropical rainfall, so a single relationship does not apply. Additionally, this method must be applied to the entire 360° azimuth, and errors arise when characteristics of the drop size distributions vary throughout the radar domain (e.g., Zrnić and Ryzhkov 1996; Ryzhkov et al. 2005b; Kumjian 2013b).

Only recently, since 2010, has the addition of dual-polarization capabilities to the WSR-88D network allowed for the evolution of precipitation processes in landfalling tropical cyclones in the continental United States to be examined in greater detail. Polarimetric radar observations allow for additional insight regarding the evolution of the drop size distribution, bulk microphysics, and number concentration of hydrometeors (e.g., Seliga and Bringi 1976; Herzegh and Jameson 1992; Zrnić and Ryzhkov 1999; Kumjian 2013a), which can be used to provide more accurate and precise Z–R relationships in heavy precipitation events associated with tropical rainfall. Dual-polarization radar also allows for the utilization of differential reflectivity (Z_{DR}) and specific differential phase (K_{DP}) to estimate rainfall rates without the assumption of an empirical Z–R relation (e.g., Ryzhkov et al. 2005b; Giangrande and Ryzhkov 2008; Cifelli et al. 2011).

In tropical environments, Houze (1997) demonstrated that precipitation in stratiform rain events is primarily driven by warm rain processes whereas convective precipitation includes additional cold rain processes when updrafts and supercooled liquid drops extend above the −10°C level (e.g., Vitale and Ryan 2013; Schroeder et al. 2016). For this reason, the warm cloud depth is defined as the layer between the cloud base and the −10°C level, to account for the presence of supercooled liquid drops that can also contribute to collision–coalescence. From Houze (1997), stratiform regions in a tropical environment can be defined as precipitation occurring in regions with weaker, decaying convection, along with the presence of a bright band in the Z_H field, which generally occurs in areas of weak ascent. Convective regions are often defined as areas of ascent greater than $1\,\mathrm{m\,s^{-1}}$ and developing young or mature convection (Houze 1997).

Robust convective features in excessive precipitation events can be identified using polarimetric radar by recognizing columns of enhanced positive Z_{DR} and/or K_{DP} extending above the 0°C level. The Z_{DR} columns indicate convective updrafts lofting supercooled drops above the melting layer in continental convection (e.g., Herzegh and Jameson 1992; Loney et al. 2002; Kumjian et al. 2014). Van Lier-Walqui et al. (2016) show that K_{DP} columns can be translated to water-coated ice or supercooled liquid being lofted above the 0°C isotherm as well.

A critical component of hydrometeorology that has not yet been explored is the relationship between polarimetric radar observations and precipitation efficiency (PE). Ye et al. (2014) define PE as the quotient of total precipitation accumulation to the total precipitable water (TPW) at the surface at the same location within a temporal period, and can be used to determine the amount of available tropospheric water vapor that can be removed from a vertical column at a given time and location (e.g., Doswell et al. 1996; Hisham Mohd Anip and Market 2007; Ye et al. 2014). Because precipitation is highly variable spatially and temporally in tropical cyclones, PE near or greater than 100% can be translated to mesoscale and storm-scale dynamic processes with large, strong updrafts that ultimately lead to condensation and heavy precipitation.

Excessive precipitation events that result in flooding typically occur where the rainfall rate is heaviest for the

longest period of time (e.g., Chappell 1986; Doswell et al. 1996). While previous studies have examined precipitation processes and hydrometeorological impacts of landfalling tropical cyclones using airborne observations, reanalysis fields, and satellite data, post-landfall Hurricane Harvey in 2017 provides a novel opportunity to specifically examine the hydrometeorological drivers of excessive precipitation and flooding using polarimetric radar observations. As such, a primary aim of this study is to quantify PE in both the convective and stratiform elements that contributed to the flooding in Houston using polarimetric radar observations from the WSR-88D network, observed radiosonde data, Multi-Radar Multi-Senor (MRMS) radar-derived rotation tracks, and North American Regional Reanalysis (NARR). The supercells that were identified in the outer rainbands of Harvey were found to have positive enhancements of the polarimetric radar variables, translating to an increase in rainfall rate and PE.

In addition, while excessive rainfall occurred across a broad region due to Harvey, isolated extreme maxima were observed within the overall precipitation swath during the event. Supercell thunderstorms are known to locally enhance rainfall rates due to their strong updrafts in the presence of rotation (Nielsen and Schumacher 2018, 2020a,b). Numerous supercells were observed in the outer rainbands of Harvey which produced 52 tornadoes, particularly in and to the south of Houston (Blake and Zelinsky 2018). Traditional supercells that develop in continental air are influenced by baroclinic instability and are known to have a PE $< 100\%$ due to the influence of hail, deep-layer shear resulting in limited drop residence time, and additional cold rain processes (e.g., Marwitz 1972; Foote and Fankhauser 1973; Browning 1977). Despite continental supercells having low PE, they are capable of producing extreme rainfall rates which can ultimately lead to flash flooding and loss of life and property (e.g., Smith et al. 2001; Duda and Gallus 2010; Hitchens and Brooks 2013). Further, supercells are able to maintain their updrafts for a longer duration compared to nonrotating storms because of the associated nonlinear hydrodynamic vertical perturbation pressure gradient force (e.g., Weisman and Klemp 1984; Doswell et al. 1996). For instance, Doswell et al. (1996) found that the intense, rotating updrafts found in supercells increase the probability for heavy rainfall rates, which would otherwise be less likely if rotation did not exist. While inferred precipitation processes using polarimetric radar observations have been analyzed in continental, midlatitude supercells (e.g., Marwitz 1972; Loney et al. 2002; Homeyer and Kumjian 2015; Nielsen and Schumacher 2018) in addition to tornadoes in tropical cyclones (e.g., McCaul 1991; Edwards 2012; Edwards et al. 2018) the polarimetric radar signatures in tropical cyclone supercells have yet to be quantified and related to QPE and precipitation processes.

Overall, the PE and excessive precipitation of supercells within a tropical cyclone environment such as Harvey have yet to be explored, thus being another novel component of this analysis. As such, this study hypothesizes that prolonged training of supercells within the outer rainbands of Harvey over Houston leads to significantly higher PE due to an environment characterized by anomalous precipitable water in addition to considerable moisture flux convergence and latent heat fluxes translating to an increase in available tropospheric moisture from condensation. Further, given Harvey's long duration and an environment characterized by anomalously high TPW and deep warm cloud depth, the combination of these elements resulted in locally excessive rainfall totals as high as 1500 mm within the extended flooding event over southeast Texas. Therefore, a secondary aim of this study is to examine the rotating features within the outer rainbands of Harvey, and their relationship to PE and enhanced rainfall rates using the available datasets in combination with MRMS radar-derived rotation tracks.

2. Data and methods

a. Event background

From 26 August 2017 to 30 August 2017, Hurricane Harvey produced over 1500 mm (60 in.) of rain in localized areas within the Houston metropolitan area with widespread precipitation accumulations of 1000 mm throughout southeast Texas (National Weather Service 2018; Fig. 1). Harvey made landfall near Rockport, Texas, at 0300 UTC 26 August as a category 4 hurricane with maximum sustained winds of 59 m s^{-1} and a minimum central pressure of 937 hPa, and produced widespread wind damage and storm surge. As Harvey progressed north, it weakened to a tropical storm by 1800 UTC 26 August before reversing track to the southeast, eventually moving back over the Gulf of Mexico at 1200 UTC 28 August. At this time, the outer rainbands from Harvey produced training convective and stratiform precipitation over Houston that led to catastrophic flooding and multiple all-time rainfall records being broken; Tropical Storm Amelia had previously held the record for the highest rainfall amount from a tropical cyclone in the continental United States, with 1219 mm in 1979 (National Hurricane Center). In contrast, during post-landfall Harvey, 18 stations across

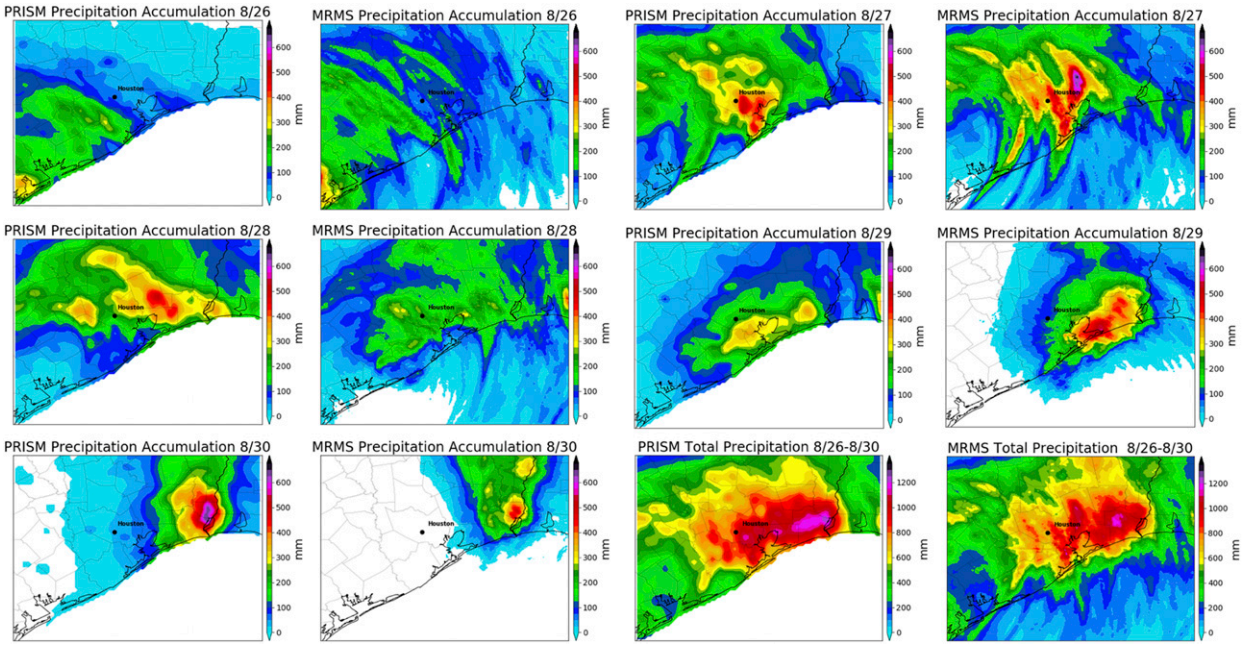

FIG. 1. A comparison between PRISM and MRMS accumulated daily precipitation from 26 to 30 Aug and total accumulated precipitation from 26 to 30 Aug.

southeast Texas reported rainfall amounts over 1219 mm during Harvey. Harvey made its final landfall over extreme southwestern Louisiana at 0800 UTC 30 August as a tropical storm before moving northeast and making a complete extratropical transition by 0600 UTC 1 September over the Tennessee Valley (Fig. 2).

b. *Reanalysis data*

The NARR dataset uses a 32-km resolution domain projected onto a Northern Hemisphere Lambert conformal conic grid (Mesinger et al. 2006) and was used in this study to calculate PE over southeast Texas. In particular, total accumulated precipitation and TPW were used from 25 to 30 August 2017 to calculate PE, which can be expressed mathematically as (1). Daily PE values from 26 to 30 August at the Corpus Christi, Texas (KCRP; 27.98686°N, 97.23364°W), and Lake Charles, Louisiana (KLCH; 30.45164°N, 92.94987°W), upper-air stations are also displayed in Table 2. PE is defined as

$$\mathrm{PE} = \frac{\text{Total precipitation accumulation}}{\mathrm{TPW}}. \qquad (1)$$

Latent heat flux anomalies were computed using the 1979–2017 climatology by removing the weekly mean from each day. These data were then standardized using the weekly standard deviation and the daily mean 10-m wind vectors were overlaid to provide an estimate of moisture advection for each day. Additionally, TPW anomalies during the same period were standardized using the daily 1979–2017 mean and standard deviation.

The Parameter-Elevation Regressions on Independent Slopes Model (PRISM) was used for daily precipitation accumulation from 26 to 30 August over southeast Texas

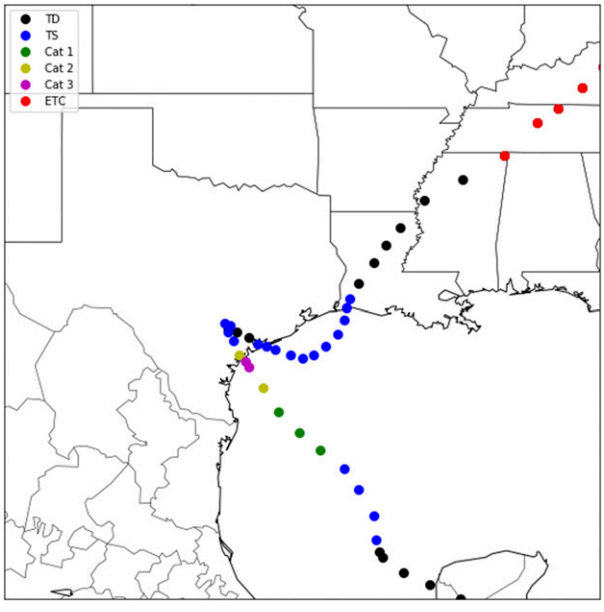

FIG. 2. Hurricane database (HURDAT) best track showing the track and categorical evolution of Harvey. Each point represents the center of circulation of Harvey. Points are spaced in 6-h time increments.

and has a 4-km grid resolution. More information regarding the data processing and projections can be found in Daly et al. (1994).

c. Polarimetric radar observations

The long duration of Harvey adjacent to the coast provided a unique opportunity to explore polarimetric radar signatures associated with a landfalling tropical cyclone given multiple NEXRAD WSR-88D radars obtained dual-polarization observations during landfall and the subsequent heavy rainfall event. The polarimetric radar data have a temporal resolution of approximately 5 min on a polar grid (Crum and Alberty 1993). The azimuthal resolution of each radar scan is 0.5° for the lowest 3–4 elevations and 1.0° otherwise. The variables analyzed in this study include Z_H, Z_{DR}, and K_{DP}. The Level-II WSR-88D data used in this study are from the National Centers for Environmental Information (Radar Operations Center 1991; Crum and Alberty 1993) and were processed using the Gridded NEXRAD WSR-88D Radar (GridRad) software (Bowman and Homeyer 2017). GridRad includes numerous quality control and filtering techniques, and merges data from multiple radars onto a grid with $0.02° \times 0.02°$ longitude–latitude resolution and a 0.5-km vertical grid spacing below an altitude of 7 km MSL and 1 km aloft (up to 22 km MSL).

The Z_H term is proportional to the integration of the diameter of scatterers raised to the sixth power (e.g., Austin 1987; Herzegh and Jameson 1992; Zrnić and Ryzhkov 1999; Kumjian 2013a; Vitale and Ryan 2013) and provides information regarding the sizes and concentrations of Rayleigh scatterers (e.g., Austin 1987; Herzegh and Jameson 1992; Zrnić and Ryzhkov 1999; Kumjian 2013a). The Z_{DR} term is defined as the difference in the horizontal and vertical reflectivity factor, and is dependent on the size, shape, and orientation of hydrometeors (e.g., Seliga and Bringi 1976; Herzegh and Jameson 1992). One must be cautious when using Z_{DR} since the measurements can be biased in the presence of mixed-phase precipitation, leading to nonuniform beam filling, as well as differential attenuation (e.g., Bringi et al. 1990; Testud et al. 2000; Ryzhkov 2007; Giangrande and Ryzhkov 2008; Kumjian 2013b,c), and radar miscalibration (e.g., Gorgucci et al. 1992; Bechini et al. 2008). The K_{DP} term is useful for determining the number concentration of raindrops in a radar volume (Kumjian 2013b). Because large raindrops are oblate, there will be more of a phase lag in the horizontal polarization relative to the vertical polarization as more media is encountered in the horizontal, yielding positive K_{DP} (e.g., Seliga and Bringi 1976; Herzegh and Jameson 1992; Zrnić and Ryzhkov 1996; Ryzhkov et al. 2005a,b; Kumjian 2013a). Last, the copolar correlation coefficient between the horizontal and vertical polarizations (ρ_{hv}) can be used to quantify the diversity of scatterers in a sample volume (e.g., Herzegh and Jameson 1992; Ryzhkov et al. 2005a,b; Kumjian 2013a). More uniform scatterers such as rain will result in a ρ_{hv} close to 1, whereas mixed-phase precipitation will yield a $\rho_{hv} < 0.9$ (e.g., Herzegh and Jameson 1992; Zrnić and Ryzhkov 1999; Ryzhkov et al. 2005a,b; Kumjian 2013a). As noted by Kumjian (2013a), Z_{DR} is independent of the number concentration of hydrometeors, but can be used in combination with K_{DP} to gain insight into the characteristics and intensity of ongoing precipitation. In the case of tropical cyclones, K_{DP} values near $1° \text{ km}^{-1}$ and Z_{DR} values between 0 and 1 dB imply a large number concentration of small drops (e.g., Brown et al. 2016; Didlake and Kumjian 2017). For this reason, regions of highest PE are expected to be largely collocated with the regions of highest Z_H, Z_{DR}, and K_{DP}, which translates to a relatively high concentration of large drops.

The K_{DP} value is computed via a centered difference method of the raw differential phase shift ϕ_{DP} observations and is then smoothed using a 7.5-km running mean to minimize noise. Additionally, grid points where $\rho_{hv} < 0.5$ are neglected as these points are largely representative of nonmeteorological scatterers. A detailed description and analysis of these algorithms can be found in Bowman and Homeyer (2017).

The 1- and 6-h means of Z_H, Z_{DR}, and K_{DP} were computed at an altitude of 2 and 3 km MSL to minimize noise from melting precipitation and bright-banding that occurred within the 4–5 km MSL layer, which acts to positively bias Z_H and Z_{DR}. This occurs because melting snowflakes gain a liquid coating on the outer portions of the crystals, which increases the overall reflectivity of the hydrometeors and therefore the Z_H (e.g., Herzegh and Jameson 1992; Ryzhkov et al. 2005a,b; Kumjian 2013a). Additionally, these melting snow aggregates results in a greater horizontal polarization compared to the vertical, and thus a highly positive Z_{DR}. The 2 and 3 km MSL levels were also chosen to minimize noise from ground clutter that is apparent in the lower 1.0 and 1.5 km MSL scans.

Time–height curtains of Z_H, Z_{DR}, and K_{DP} from 26 to 30 August are computed using 1) a five-data-point radius around Houston, Texas, with a latitude and longitude of 29.7396°N and 95.3854°W, and 2) a five-data-point radius around Liberty, Texas, with coordinates of 30.0554°N and 94.7932°W. A spatial mean over the five surrounding grid points was used for plotting, similar to the quasi-vertical profile methodology of Ryzhkov et al. (2016). These points were subjectively chosen to gain insight to the vertical distribution polarimetric radar

variables, and how they varied spatially between different portions of the outer rainbands of Harvey during periods of exceptional precipitation.

Raw NEXRAD-WSR 88D radar data from the Houston radar (KHGX) were used to plot a single-site radar image of 0.5° Z_H and 3–6-km MRMS azimuthal shear from 0301 to 0401 UTC 27 August. The azimuthal shear field was derived from the raw 0.5° radial velocity field as described by Smith and Elmore (2004).

Radar-derived rainfall rates and precipitation accumulations were derived using the $R(K_{DP}, Z_{DR})$ relationship from Zhang et al. (2018) and described in Eq. (2). This quantitative precipitation estimation (QPE) algorithm was found to perform best when $Z_H \geq 38$ dBZ, $K_{DP} \geq 1° \text{km}^{-1}$, and $Z_{DR} \geq 1$ dB, using the constants $a = 51.16$, $b = 0.9311$, and $c = -0.0852$, which are empirically derived and are best used in convective, warm rain events (Zhang et al. 2018). The 1-h rainfall rates were computed using the 1-h means of Z_H, Z_{DR}, and K_{DP} at 2 km, and 6-h mean rainfall rates were also calculated by averaging the 1-h mean rainfall rates over the 6-h periods. Finally, a Z_{DR}- and K_{DP}-weighted drop size estimation for convective, tropical rainfall (Gorgucci et al. 2002) was used to estimate the mean drop diameter within the supercells embedded in the outer rainbands of Harvey from 0300 to 0400 UTC 27 August and is expressed in (3):

$$R(K_{DP}, Z_{DR}) = aK_{DP}^{b}10^{cZ_{DR}}, \quad (2)$$

$$\hat{D}_o = 1.155(K_{DP})^{0.076}(Z_{DR})^{1.164}. \quad (3)$$

d. MRMS radar-derived rotation tracks and gauge-corrected precipitation data

The MRMS (NOAA/National Severe Storms Laboratory) radar-derived rotation tracks were incorporated into the 1-h mean Z_H plots to quantify the correlation between rotation tracks associated with the tropical supercells and enhanced Z_H. Rotation tracks were derived from the azimuthal shear field from the KHGX radar and are obtained by using a linear least squares derivative method (e.g., Smith and Elmore 2004; Smith et al. 2016) on the radial velocity from the radar site. The tracks have a temporal resolution of 2 min, with a spatial resolution of 555 m × 504 m. Further, both 0–2- and 3–6-km rotation tracks were analyzed to examine the low-level and midlevel rotation associated with these supercells. The rotation track data used the 60-min data within each hour to represent the swaths of enhanced azimuthal shear that occurred within the previous hour. The tracks were then superimposed atop 1-h mean values of the polarimetric radar variables. Only values above $0.016\,\text{s}^{-1}$ were displayed to minimize noise and isolate supercellular features.

MRMS gauge bias corrected QPE was used to quantify precipitation accumulation over southeast Texas from 26 to 30 August and was compared to the PRISM rainfall accumulations as a source for verification. The MRMS gauge bias corrected QPE quality controls for gauge biases and errors, and uses an inverse distance weighting scheme to interpolate between gauge locations to map the precipitation field. More information regarding the algorithm used to derive the MRMS gauge-corrected QPE can be found in Zhang et al. (2011).

e. Additional data

The hurricane database (HURDAT) best track data (SAIC et al. 1993) were used to plot the track and varying intensity of Harvey through its entire evolution (Fig. 2). Each data point has a 6-h temporal resolution, which represents the center of circulation of Harvey. Sea surface temperature magnitudes and anomalies were computed using the NOAA Optimum Interpolation Sea Surface Temperature v2 dataset available on a 1° × 1° global longitude–latitude grid (Reynolds et al. 2002). The anomalies were computed by subtracting the monthly mean from each day since SSTs generally vary over a time scale larger than one day due to their high specific heat capacity (Fig. 3).

Filtered storm reports from the Storm Prediction Center (SPC) were used to identify locations of tornado reports associated with the outer rainbands of Harvey from 26 to 28 August. Finally, observed radiosonde data from the Corpus Christi, Texas (KCRP), and Lake Charles, Louisiana (KLCH), upper-air sites were plotted from 0000 UTC 26 August through 1200 UTC 28 August using MetPy plotting software (May et al. 2017). These upper-air observations were used to calculate the warm cloud depth consistent with the methodology used by Vitale and Ryan (2013). Table 1 shows daily mean values of TPW, with the anomalies calculated from the Storm Prediction Center sounding climatology (NOAA/NWS SPC) using the 1989–2014 mean TPW at KCRP and the 1948–2014 climatology at KLCH.

3. Results

a. Precipitation efficiency

During the 6-day period in which Harvey was located over southeast Texas, TPW anomalies largely exceeded 1.5σ–2.5σ (Fig. 4). These values are consistent with observed radiosonde data from KCRP (Fig. 5) and KLCH (Fig. 6), shown in Table 1. Here, moist adiabatic

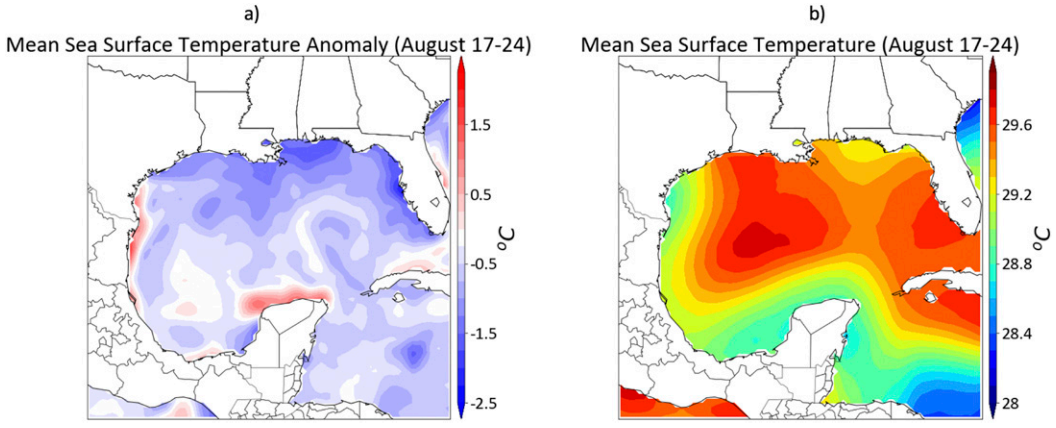

FIG. 3. (a) Mean sea surface temperature anomaly from 17 to 23 Aug and (b) mean sea surface temperature from 17 to 23 Aug, for the week prior to Harvey making landfall.

tropospheric profiles throughout the period were observed with "skinny" convective available potential energy (CAPE) (e.g., Davis 2001; Jessup and DeGaetano 2008; Schroeder et al. 2016). Skinny CAPE profiles are indicative of slow ascent rates at lower altitudes and a longer cloud droplet residence time compared to the "fat" CAPE profiles that are typically associated with midlatitude, continental supercells (e.g., Vitale and Ryan 2013; Schroeder et al. 2016), translating to a likely more efficient drop growth process via collision–coalescence.

Additionally, a deeper warm cloud depth maximizes the vertical extent of warm rain processes, which further act to maximize PE at the surface (Hisham Mohd Anip and Market 2007). Table 2 shows how the warm cloud depth varied throughout the evolution of Harvey, with warm cloud depth values consistently in excess of 6000 m from 26 to 30 August. Further, it can be seen from Fig. 7 that the areas of maximum PE were largely collocated with the central location of Harvey. While PE typically ranges from 0% to 100%, PE can exceed 100% due to horizontal moisture flux convergence and latent heat fluxes, which adds moisture to the vertical column through horizontal and vertical moisture advection and condensation. This is confirmed via Fig. 8 which displays the significant latent heat fluxes over southeast Texas that acted to increase total column water vapor. Because the sign of the flux is dependent on direction, a negative latent heat flux corresponds to a downward moisture flux, which ultimately results in condensation and vast amounts of latent heat release. The regions of latent heat flux anomalies which exceeded -3σ relative to climatology were primarily located upstream of the areas of enhanced PE. The mean 10-m wind vectors are overlaid to provide a qualitative sense of the ongoing moisture advection over the region, acting to increase the amount of available water vapor in the vertical column. Additionally, Fig. 9 illustrates the collocation of positive horizontal moisture flux convergence anomalies with regions of enhanced PE. However, the highest horizontal moisture flux convergence anomalies are offset from the regions of highest PE particularly from 26 to 27 August. This may be due to the inner core of Harvey maximizing convergence at the center of circulation, which remained to the west of Houston during this period.

Tables 1 and 2 demonstrate the relationship between PE, TPW anomalies, and warm cloud depth. The greatest TPW anomaly, PE, and warm cloud depth were temporally collocated at KCRP on 26 August. Additionally, the greatest TPW anomaly at KLCH was temporally offset from the times of highest PE and deepest warm cloud depth by one day. However, qualitatively there exists a positive relationship between positive TPW anomalies, warm cloud depth greater than 6000 m, and PE greater than 100%. This demonstrates that anomalously high total column water vapor and deep warm cloud depths

TABLE 1. Observed TPW (mm), observed TPW anomalies (mm), and NARR TPW (mm) from 26 to 30 Aug at KCRP and KLCH.

Date	KCRP TPW	KCRP TPW anomaly	KCRP NARR	KLCH TPW	KLCH TPW anomaly	KLCH NARR
26 Aug	68.89	22.92	62.08	62.82	17.86	58.31
27 Aug	64.66	19.70	59.95	65.23	20.53	60.01
28 Aug	56.41	11.20	56.19	63.73	18.52	57.67
29 Aug	48.27	2.55	52.39	57.61	12.14	55.06

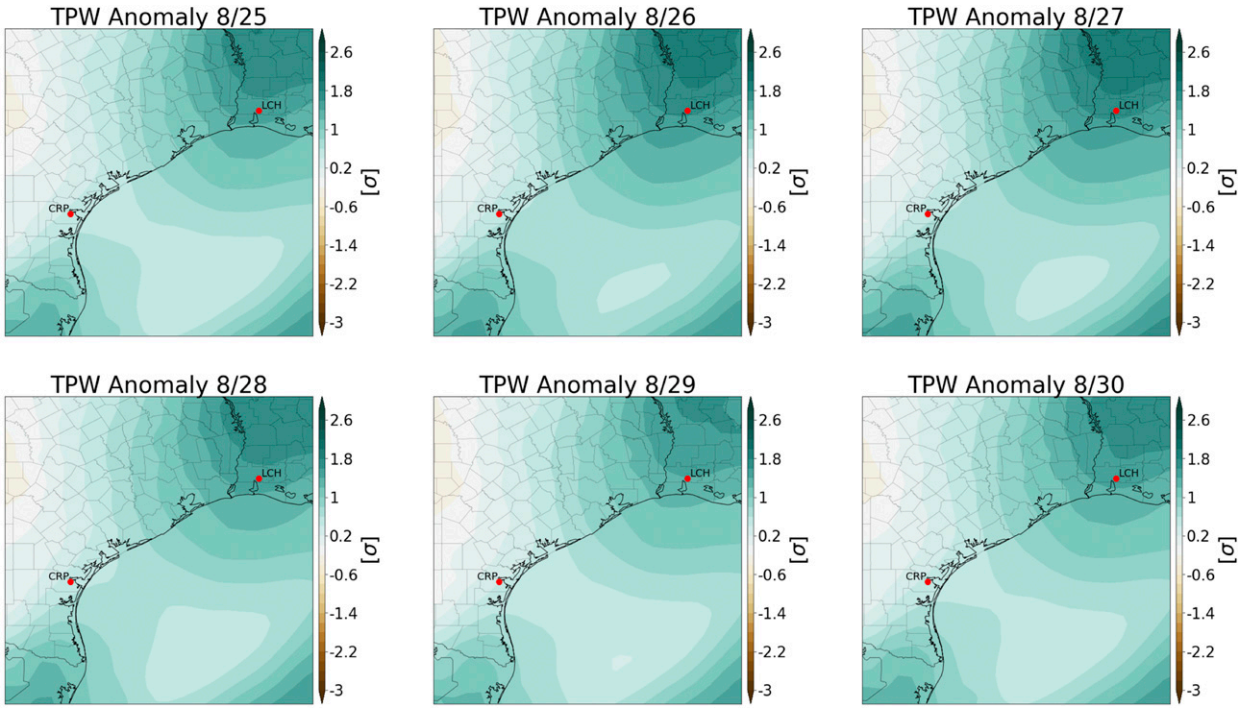

FIG. 4. Total precipitable water (TPW) anomaly from 25 to 30 Aug standardized from the 1979– 2017 climatology.

maximized the extent of warm rain processes and acted to enhance PE at the surface.

b. *Polarimetric radar analysis*

Figure 10 displays the 6-h mean values of Z_H, Z_{DR}, and K_{DP} at 3 km over Houston from 27 to 28 August. The mean Z_H values ranged from 35 to 45 dBZ to the north of Houston and from 20 to 30 dBZ to the south. A similar spatial pattern existed with Z_{DR}, with values exceeding 1 dB to the north of Houston, and values between 0 and 0.5 dB to the south. In addition, notable swaths of 6-h mean K_{DP} exceeding $1°\,km^{-1}$ occurred

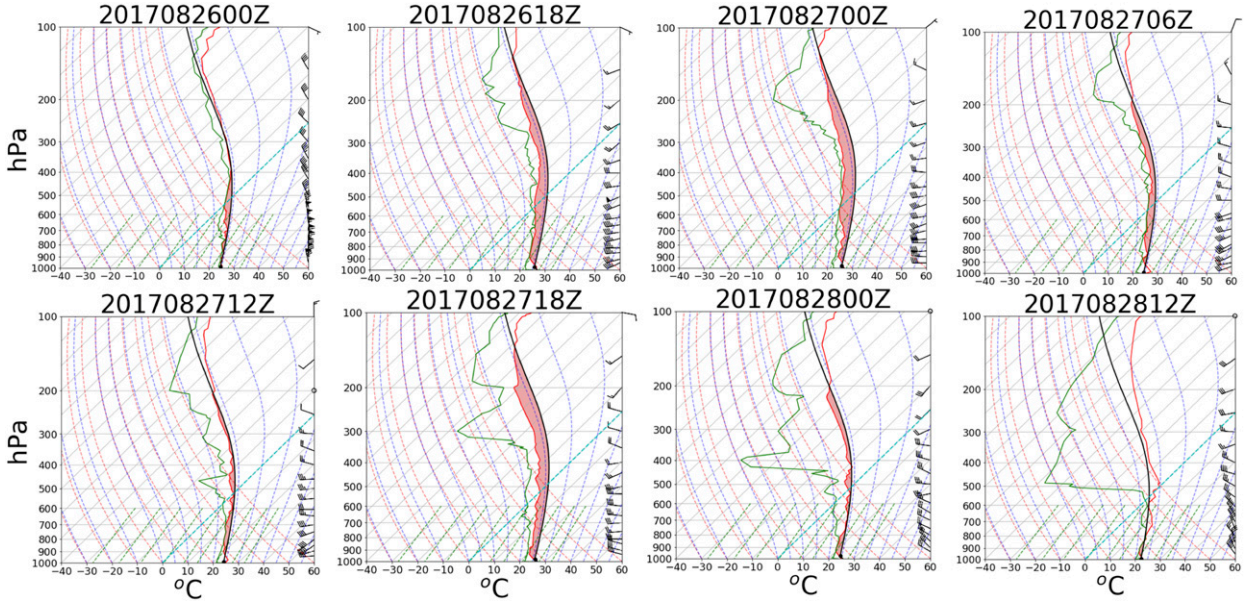

FIG. 5. Observed soundings taken over KCRP from 0000 UTC 26 Aug to 1200 UTC 28 Aug.

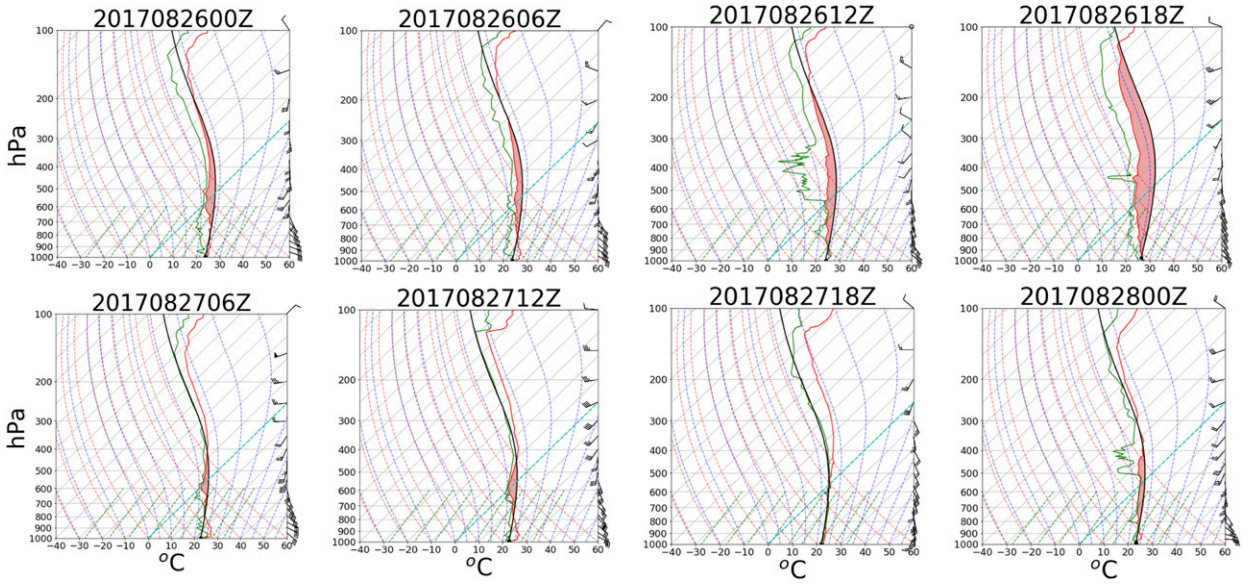

FIG. 6. Observed soundings taken over KLCH from 26 to 28 Aug.

over the same regions experiencing the enhanced positive Z_H and Z_{DR}. The combination of these polarimetric radar variables implies a larger number concentration of larger drops in a sample volume to the north of Houston compared to the south. Although the larger values of Z_{DR} in the northern area of Houston imply the presence of larger drops and perhaps some contamination from melting precipitation, Z_{DR} of 1–1.5 dB is still characteristic of small drops and warm rain (e.g., Squires 1956; Ulbrich and Atlas 2008; Carr et al. 2017). In addition, this region was spatially collocated with PE exceeding 100%. This overall pattern was also observed from 28 to 29 August across the region with slightly lower values of all three variables as compared to 27 August (figure not shown).

A time–height curtain of Z_H, Z_{DR}, and K_{DP} over Houston from 27 to 28 August to provides insight into the vertical extent of precipitation processes (Fig. 11). These profiles help identify dynamic features such as the melting layer height and columns of enhanced Z_{DR} and K_{DP} extending above the melting layer, implying robust convective updrafts. From 27 to 28 August, Z_H exceeded 45 dBZ for more than half the period. This was not surprising given Houston received nearly 500 mm of rain on this day, with a maximum in PE exceeding 300% located over the city and extending to the north and west. Similarly, numerous Z_{DR} columns coexisted with the regions of high Z_H and Z_{DR} up to 1.5 dB. A similar pattern existed in the K_{DP} field, implying a large concentration of larger drops was being lofted above the melting layer. An upward displacement of the melting layer was also observed coincident with convection over the area that acted to increase the warm cloud depth and increase PE at the surface.

One interesting difference in the polarimetric radar fields exists over Liberty from 29 to 30 August (Fig. 11). The Z_H field ranges from 20 to 40 dBZ and is characteristic of stratiform precipitation. From 0600 to 1200 UTC, Z_{DR} ranges from 0 to 1 dB, and K_{DP} ranges from 0 to 0.5° km^{-1} below the melting layer, which is indicative of a larger number concentration of small drops, and is expected in an environment with a deep warm cloud depth. From 1800 to 0000 UTC, similar values of Z_H remained over the region, however Z_{DR} was much larger, with values between 1 and 2 dB, whereas K_{DP} was near 0° km^{-1}. This is consistent with a small number concentration of large drops, and more characteristic of midlatitude, continental precipitation that involves additional cold rain processes.

These vertical profiles also infer information regarding whether drop evolution was dominated by coalescence or breakup. An increase in Z_{DR} toward the ground would imply collision–coalescence was the dominant process as an increase in drop size results in raindrops becoming increasingly oblate with a greater

TABLE 2. Warm cloud depth (WCD) (m) and PE (%) from 26 to 30 Aug at KCRP and KLCH.

Date	KCRP WCD	KCRP PE	KLCH WCD	KLCH PE
26 Aug	6950	114.7	6350	17.9
27 Aug	6248	3.6	6428	98.7
28 Aug	6460	5.6	5940	267.5
29 Aug	6144	1.0	6401	56.4

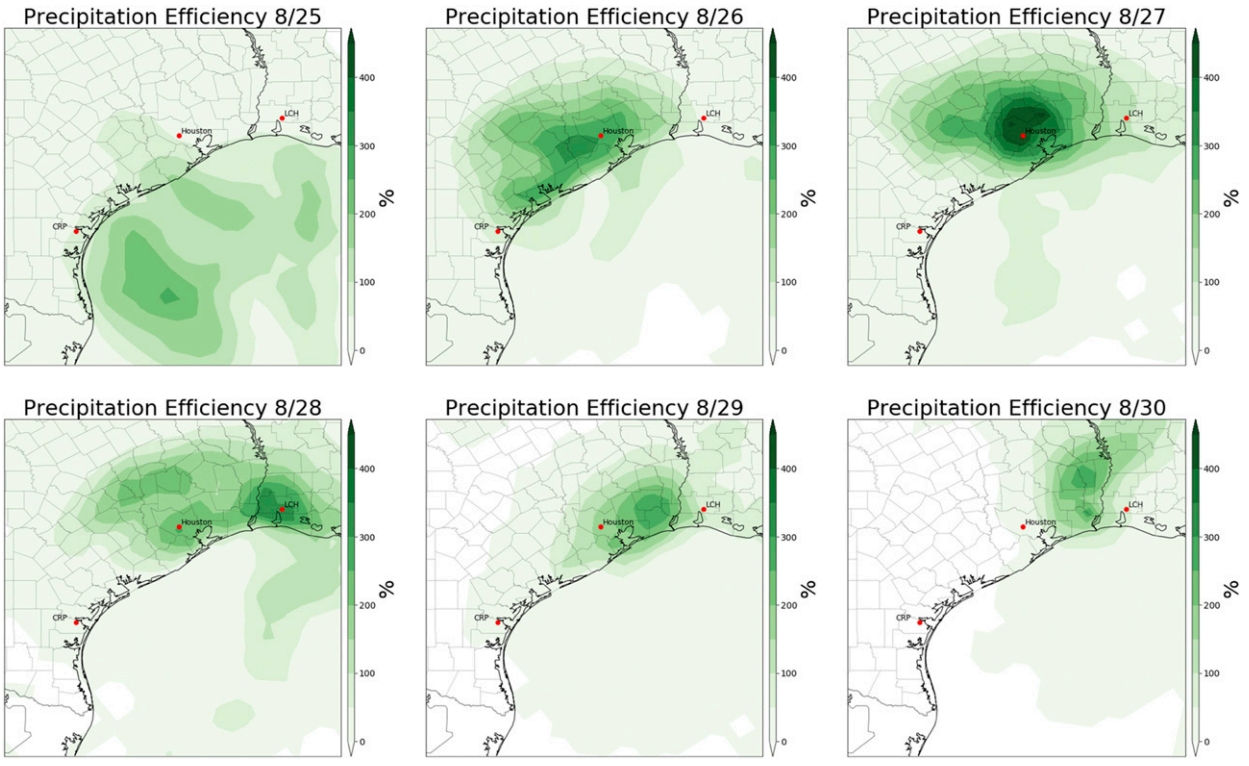

FIG. 7. Precipitation efficiency (PE) calculated using (1) from 25 to 30 Aug.

horizontal dimension when compared to the vertical (e.g., Kumjian 2012; Carr et al. 2017). Similarly, a decrease in Z_{DR} and increase in Z_H toward the surface implies a balance between drop breakup and collision–coalescence (e.g., McFarquhar and List 1991; Kumjian 2012; Carr et al. 2017). Figure 12 shows 6-h means of the vertical profiles of Z_H, Z_{DR}, K_{DP}, and ρ_{hv} over Houston from 27 to 29 August. From 27 to 28 August, Z_{DR} decreased toward the surface except for the 0600–1200 UTC time frame, yet Z_H increased toward the ground. This decrease in Z_{DR} and increase in Z_H with decreasing height is reflective of a balance between collision–coalescence and drop breakup. However, from 0000 to 0012 UTC 28–29 August, Z_{DR} increased toward the surface. This is characteristic of collision–coalescence dominating breakup and is expected to occur in a tropical cyclone environment.

c. *Rotation track analysis*

The 1-h mean values of Z_H at 2 km were also analyzed for the study domain and Fig. 13 reveals swaths of enhanced Z_H of approximately 50–55 dBZ over Houston. The hourly MRMS 3–6-km rotation was overlaid for the same period to determine whether supercells within the outer rainbands and the swaths of enhanced Z_H were present and producing excessive precipitation. From 0300 to 0400 UTC on 27 August, training supercells moving northward off the Gulf of Mexico were located over eastern portions of Houston and yielded swaths characterized by 1-h mean values of Z_H near 50 dBZ, values of Z_{DR} between 1 and 1.5 dB, and K_{DP} values of 1.5°–2° km^{-1}. This is consistent with a larger average drop size within a sample volume in relation to the larger-scale mean Z_{DR} distribution and is consistent with the spatial correlation between a large number concentration of larger drops within a radar volume being collocated with the highest values of PE. This is different than the lower PE associated with midlatitude, continental convection. Additional training supercells occurred from 0600 to 0700 UTC 28 August east of Liberty with Z_H values near 45 dBZ, Z_{DR} values near 1.5 dB, and maximum K_{DP} values of 1.5° km^{-1}. The overlaid azimuthal shear shows that the convective elements over these locations were also rotating, implying that supercells were responsible for producing these enhanced values of Z_H, Z_{DR}, and K_{DP}.

d. *Quantitative precipitation estimation in tropical supercells*

Figure 14 shows the 1-h mean rainfall rates within these training supercells were estimated to be as high as 85 mm h^{-1}, with widespread rainfall rates exceeding

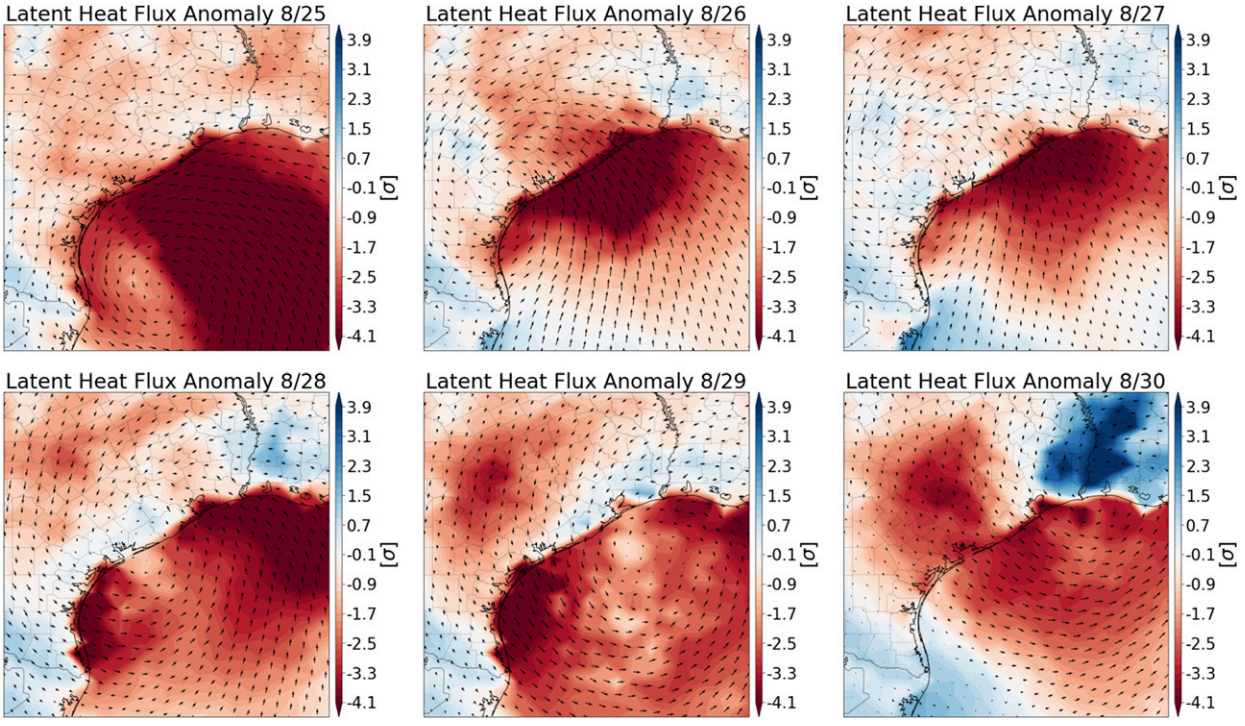

FIG. 8. Latent heat flux anomalies from 25 to 30 Aug standardized from the 1979–2017 climatology, with daily mean 10-m wind vectors.

50 mm h^{-1} within the line of supercells from 0300 to 0400 UTC 27 August, extending 85 km inland from the coast. When averaged over the 0000–0600 UTC time frame, the 6-h mean rainfall rates were estimated to be as high as 45 mm h^{-1} to the southeast of Houston where the training supercells in the outer bands were occurring. This translates to 6-h rainfall accumulations nearing 250 mm over the same area. Further, throughout the

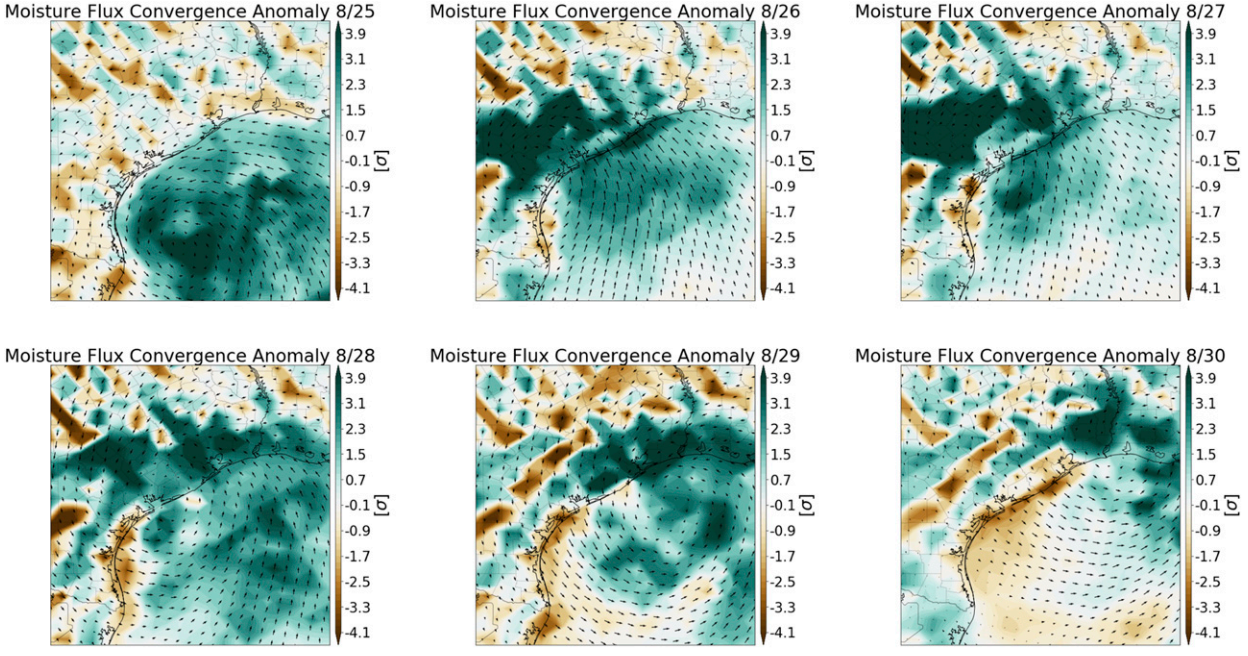

FIG. 9. Moisture flux convergence anomalies from 25 to 30 Aug standardized from the 1979–2017 climatology, with daily mean 10-m wind vectors.

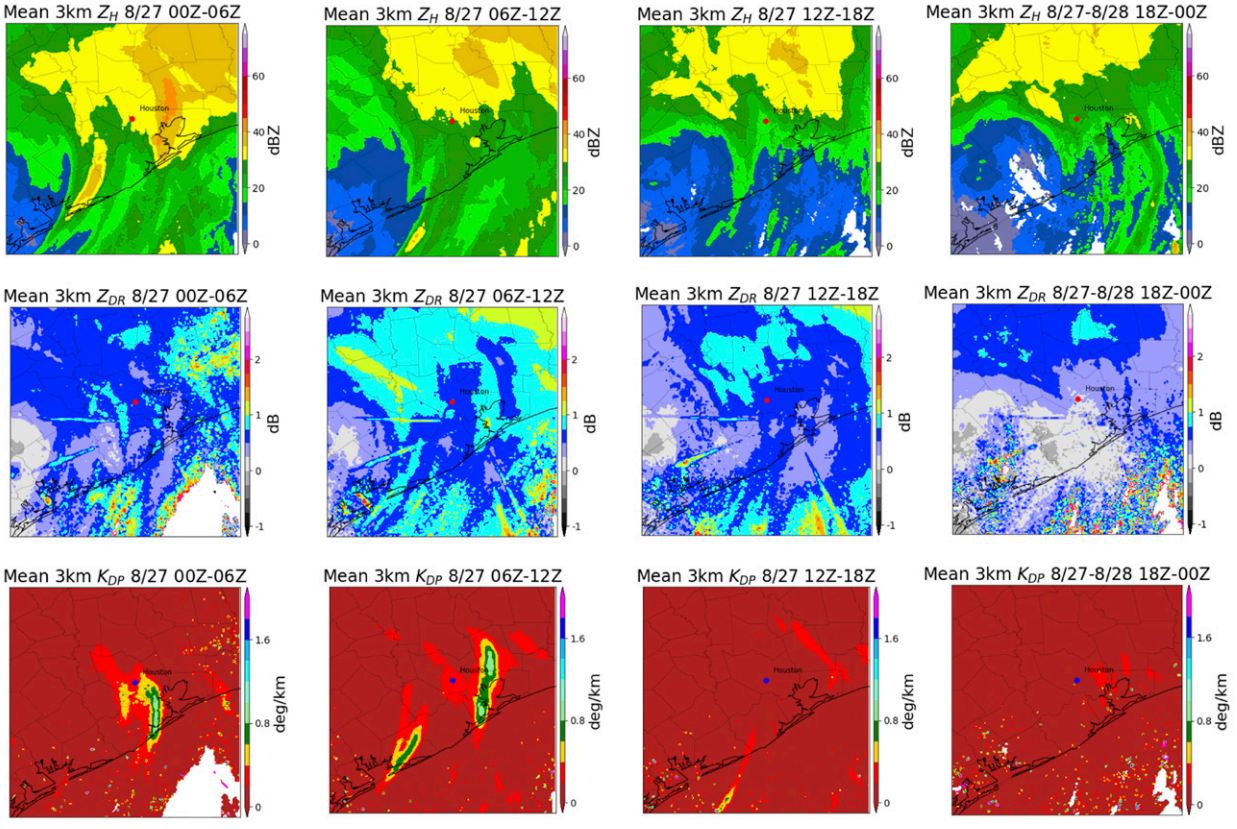

FIG. 10. The 6-h means of 3-km Z_H, Z_{DR}, and K_{DP} from 26 to 27 Aug.

24 h period, this $R(K_{DP}, Z_{DR})$ relationship estimated rainfall accumulations as high as 425 mm, with widespread rainfall totals of 200–400 mm over the region where training supercells did not occur. The Z_{DR}- and K_{DP}-weighted drop size estimation that was used to quantify the mean drop size shows drops exceeding 2 mm in diameter within the supercells. This is substantially larger than the drops within the stratiform precipitation of Harvey, which generally ranged from 0.5 to 1 mm in diameter.

4. Discussion

Landfalling tropical cyclones produce excessive rainfall that can lead to catastrophic flooding, especially if steering flow is weak and the remnant TC remains stationary for an extended period of time (Rappaport 2000). Even after TCs become less organized and lose their compact circulation as they move inland, the deadliest hazard is often freshwater flooding such as occurred during Tropical Storms Charley (1998), Alberto (1994), and Amelia (1978) (Rappaport 2000).

Excessive rainfall occurs where rain is heaviest for the longest period of time (Doswell et al. 1996). A synoptic-scale environment characterized by high TPW and large precipitation accumulation at the surface yields a high PE (Ye et al. 2014). Because the large-scale environment over southeast Texas from 25 to 31 August yielded TPW anomalies exceeding 1.5σ–2.5σ, Harvey remained quasi-stationary in a region conducive for enhanced PE. As such, observed rainfall totals were greater than 1000 mm over a region spanning nearly 40 000 km^2.

Given the extended duration of the event and the proximity of Harvey to the KHGX WSR-88D, polarimetric radar observations of Z_H, Z_{DR}, and K_{DP}, were used to quantify precipitation processes in the outer rainbands. The polarimetric radar observations were able to capture the evolution and extent of the warm rain processes that contributed to the excessive rainfall event over southeast Texas. Widespread values of Z_H greater than 30 dBZ existed over the Houston area from 27 to 29 August. However, Z_H alone does not reveal much about the hydrometeor size, shape, and orientation (e.g., Seliga and Bringi 1976; Herzegh and Jameson 1992; Ryzhkov et al. 2005a,b; Kumjian 2013a), which can provide information about the ongoing precipitation processes (Didlake and Kumjian 2017). However, when combining the Z_H field with the

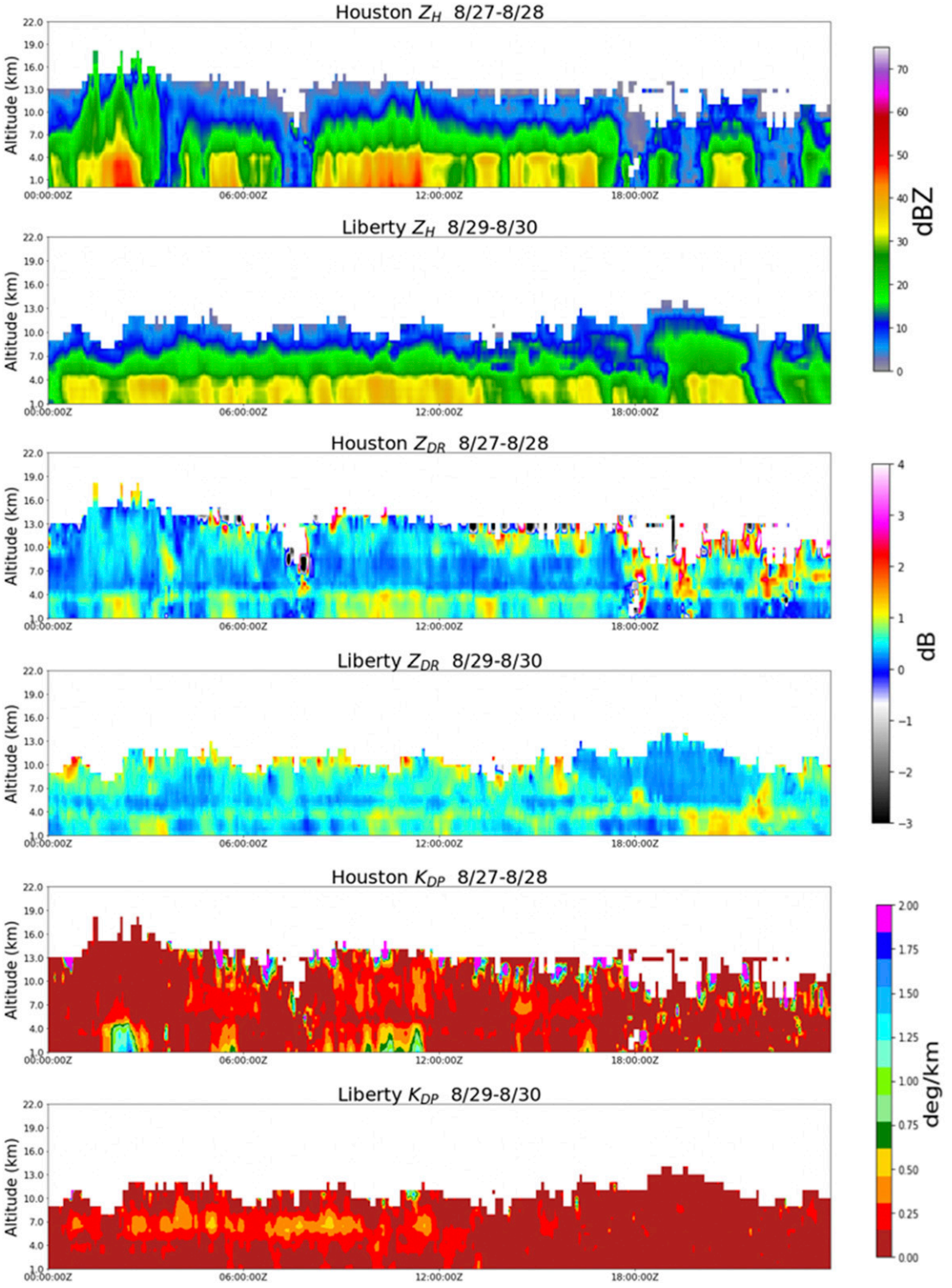

FIG. 11. Time–height curtains of Z_H, Z_{DR}, and K_{DP} over Houston, Texas, from 27 to 28 Aug and over Liberty, Texas, from 29 to 30 Aug.

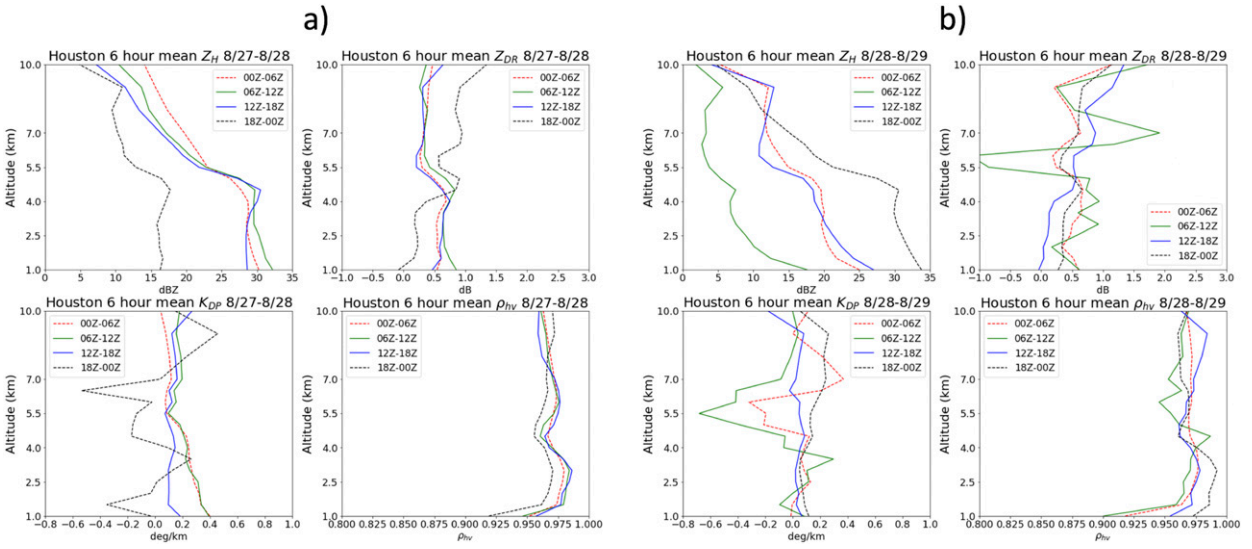

FIG. 12. The 6-h mean vertical profiles of Z_H, Z_{DR}, K_{DP}, and ρ_{hv} over Houston (a) from 27 to 28 Aug and (b) from 28 to 29 Aug.

observed 6-h mean Z_{DR} values near 0.5 dB and 6-h mean K_{DP} values of 0.5° km^{-1}, the results yield a large concentration of small drops that contributed to the excessive precipitation event over southeast Texas. The synoptic-scale environment and resultant aforementioned Z_H, Z_{DR}, and K_{DP} values that resulted in high PE were conducive to an excessive precipitation event that produced widespread rainfall totals 100–200 mm over southeast Texas from 27 to 28 August.

While widespread rainfall rates of 10–20 mm h^{-1} occurred due to the anomalously moist conditions on the synoptic scale, the heaviest rainfall rates and precipitation totals occurred within training supercells in the outer rainbands of Harvey. Polarimetric radar observations also provide useful information regarding enhanced rainfall rates in convective storms through identification of Z_{DR} and K_{DP} columns (Homeyer and Kumjian 2015). These columns of enhanced Z_{DR} and K_{DP} can identify large supercooled drops being lofted above the freezing level by convective updrafts (e.g., Herzegh and Jameson 1992; Loney et al. 2002; Kumjian et al. 2014) and can help distinguish embedded convective features from stratiform elements within the outer rainbands (e.g., Griffin et al. 2014; Didlake and Kumjian 2018).

The supercells in Harvey were identified using 3–6-km MRMS rotation tracks and were collocated with swaths of enhanced polarimetric radar variables. Within these supercells from 0300 to 0400 UTC 27 August, the 1-h mean values of Z_H, Z_{DR}, and K_{DP} were as high as 50 dBZ, 1.25 dB, and 2° km^{-1}, respectively. These results are consistent with those in Nielsen and Schumacher (2018), where mesocyclones were found to be responsible for enhanced rainfall rates at the surface during a rainfall event in central Texas. Figure 15 shows the training nature of the supercells that acted to increase the temporal component of flooding via the locally enhanced PE and rainfall rates. The $R(K_{DP}, Z_{DR})$ relationship highlights a swath of 1-h mean rainfall rates as high as 85 mm h^{-1} associated with the training supercells. When examining the 6-h mean rainfall rate, the localized swath of 40–45 mm h^{-1} rainfall rates southeast of Houston can be identified within the widespread area of 10–20 mm h^{-1} rainfall rates that can be attributed to the large-scale environment that was favorable for excessive rainfall coincident with the training supercells. Additionally, numerous instances of supercell mergers occurred within the outer rainbands from 0200 to 0400 UTC 27 August, which acts to merge two different drop size distributions and increase precipitation efficiency (e.g., Marwitz 1972; Markowski and Richardson 2010).

Overall, supercells within the outer rainbands of Harvey were determined to be responsible for two localized swaths of rainfall accumulations of 300–400 mm above the synoptically driven precipitation conditions. This is consistent with Nielsen and Schumacher (2018) who demonstrated that extreme rainfall accumulations are often closely collocated with mesovortices in midlatitude supercell thunderstorms. One reason that supercells are often responsible for excessive precipitation is that they contain a sustained source for ascent via nonlinear dynamic perturbation pressure gradient forces (e.g., Weisman and Klemp 1984; Doswell et al. 1996). Newton (1966) hypothesized that PE is enhanced in deep, saturated vertical columns, limiting dry air entrainment and therefore evaporation. Thus, given this

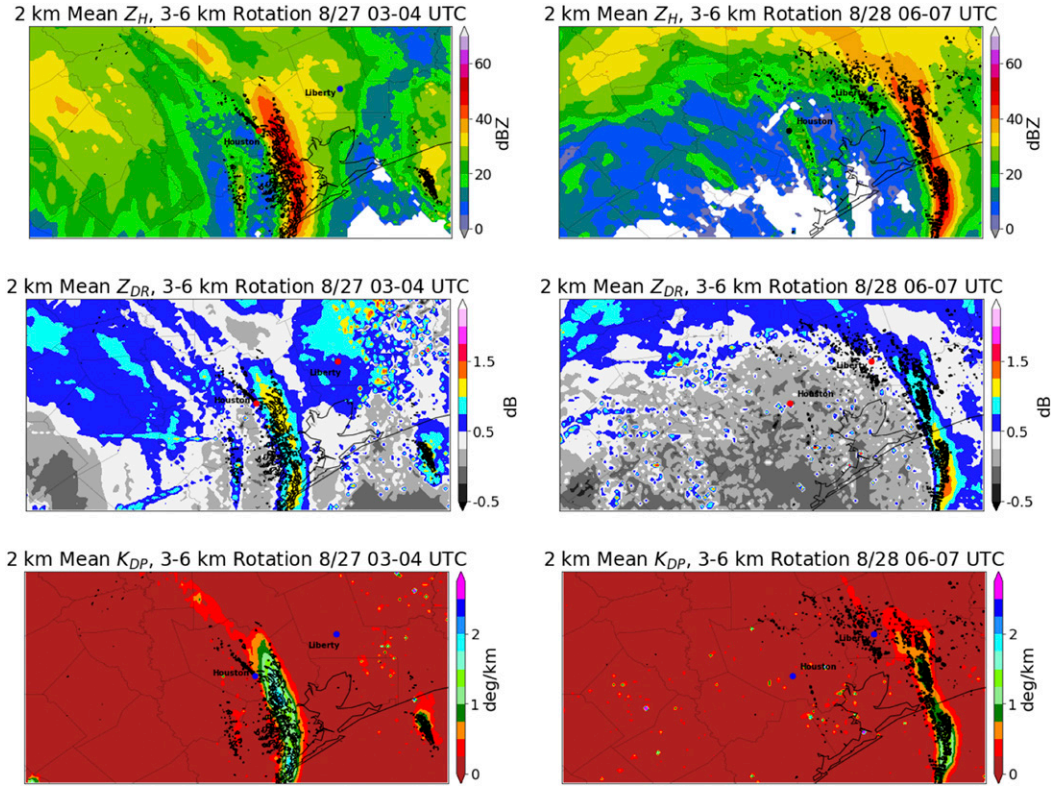

FIG. 13. The 1-h means of 2-km Z_H, Z_{DR}, and K_{DP} (a) from 0300 to 0400 UTC 27 Aug and (b) from 0700 to 0800 UTC 28 Aug, with 3–6-km hourly rotation tracks greater than 0.016 s^{-1} (contours).

convection contained sustained, rotating updrafts in an area of enhanced TPW and PE, the resultant training supercells substantially contributed to the most catastrophic rainfall that occurred over Houston.

Limitations

Coarsely spaced radiosonde observations and reanalysis data used to quantify TPW introduces some limitations when relating PE to a high temporal resolution dataset such as the NEXRAD WSR-88D polarimetric radar observations. Because PE is dependent on TPW, it would be useful to obtain hourly measurements of TPW to perform hourly spatial distributions of PE. This would allow for a more precise spatial correlation of PE and means of polarimetric radar variables.

One potential issue arises when compositing polarimetric radar variables close to the surface, as ground clutter can often bias these observations and obscure the meteorological signals. This can be problematic since PE is calculated using accumulated precipitation observations at the surface, whereas the radar observations are analyzed at 2–3 km above ground level to avoid contamination from nonmeteorological scatterers. Future analyses could remove these artifacts by setting a threshold greater than 0.5 for ρ_{hv}, as precipitation in tropical cyclones tends to be uniform in size, yielding ρ_{hv} near 1 in the absence of melting precipitation.

A limitation to the QPE method is that it does not perform well in areas of light rain, which did occur in between supercells and outer rainbands. Another constraint is that the rainfall rate at 2 km may actually be an underestimation of the rainfall rate at the surface. This is because of additional drop growth toward the ground, which is due to collision–coalescence and results in an increase in Z_{DR} and K_{DP}.

5. Conclusions

Excessive precipitation occurred over southeast Texas from Harvey and over 1000 mm of rain fell from 26 to 30 August, resulting in catastrophic urban and river flooding along with the loss of life and property. The heaviest precipitation totals typically collocate with regions that experience the heaviest precipitation for the longest period of time. Harvey remained nearly stationary over Houston and southeast Texas for 4 days, leading to a long duration excessive precipitation event. This study combined multiple datasets in a novel manner during an unprecedented precipitation

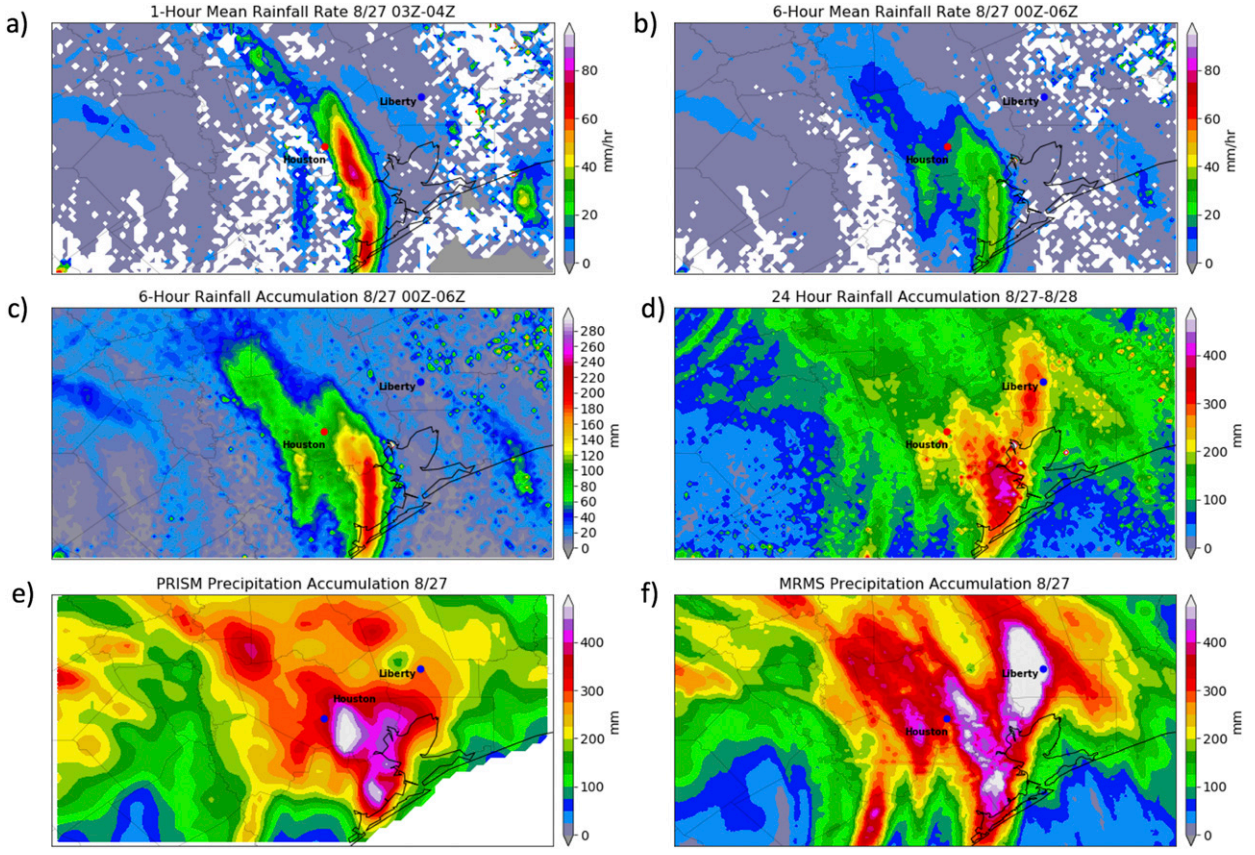

FIG. 14. (a) The 1-h mean rainfall rate from 0300 to 0400 UTC 27 Aug and (b) 6-h mean rainfall rate from 0000 to 0600 UTC 27 Aug using the aforementioned $R(K_{DP}, Z_{DR})$ relationship, rainfall accumulation (c) from 0000 to 0600 UTC 27 Aug and (d) from 0000 UTC 27 Aug to 0000 UTC 28 Aug, and (e) 27–28 Aug rainfall accumulation from PRISM and (f) 27–28 Aug rainfall from MRMS.

event to 1) examine the multiscale linkages driving PE and 2) the role of tropical supercells and local extremes in rainfall.

During the Harvey period, TPW anomalies exceeded 1.5σ–2.5σ above the mean climatological value occurred throughout this period. Further, the PE $>$ 100% resulted from enhanced warm rain processes in addition to anomalously high horizontal moisture flux convergence, and negative latent heat flux anomalies (condensation), which increased the overall available moisture content in the vertical column.

When incorporating polarimetric radar observations from the NEXRAD WSR-88D network, 6-h temporal means of Z_H, Z_{DR}, and Z_{DP} at 3 km from 27 to 28 August show the highest values of all three variables located to the north and west of Houston, with a mean Z_H of 35–45 dBZ, a mean Z_{DR} of 1–1.5 dB, and a mean K_{DP} near $1^\circ\,km^{-1}$. This is largely collocated with the highest values of PE during the same period, and is reflective of a relatively large number concentration of larger drops. While the drop size is larger in this region compared to areas to the south and east of Houston, this is still characteristic of small drops, which is expected in a tropical cyclone environment.

Time–height cross sections of these polarimetric variables over Houston also show columns of enhanced Z_H, Z_{DR}, and K_{DP} extending above the melting layer. This translates to convective updrafts lofting oblate hydrometeors above the freezing level, which results in a greater PE at the surface. Finally, 6-h mean vertical profiles of these profiles in addition to ρ_{hv} over Houston show Z_{DR} increasingly toward the surface below the melting layer. This is indicative of drop growth via collision–coalescence.

Additionally, swaths of 3–6-km rotation tracks were largely collocated with swaths of enhanced positive Z_H, Z_{DR}, and K_{DP}, implying that these supercells produced a large number concentration of large drops compared to the surrounding environment. The high PE in these supercells is contrary to the low PE that is typically found in midlatitude, continental supercells. However, these supercells within the outer bands of Harvey produced 1-h mean rainfall rates of up to $85\,mm\,h^{-1}$ and were critical drivers of the localized extremes of rainfall

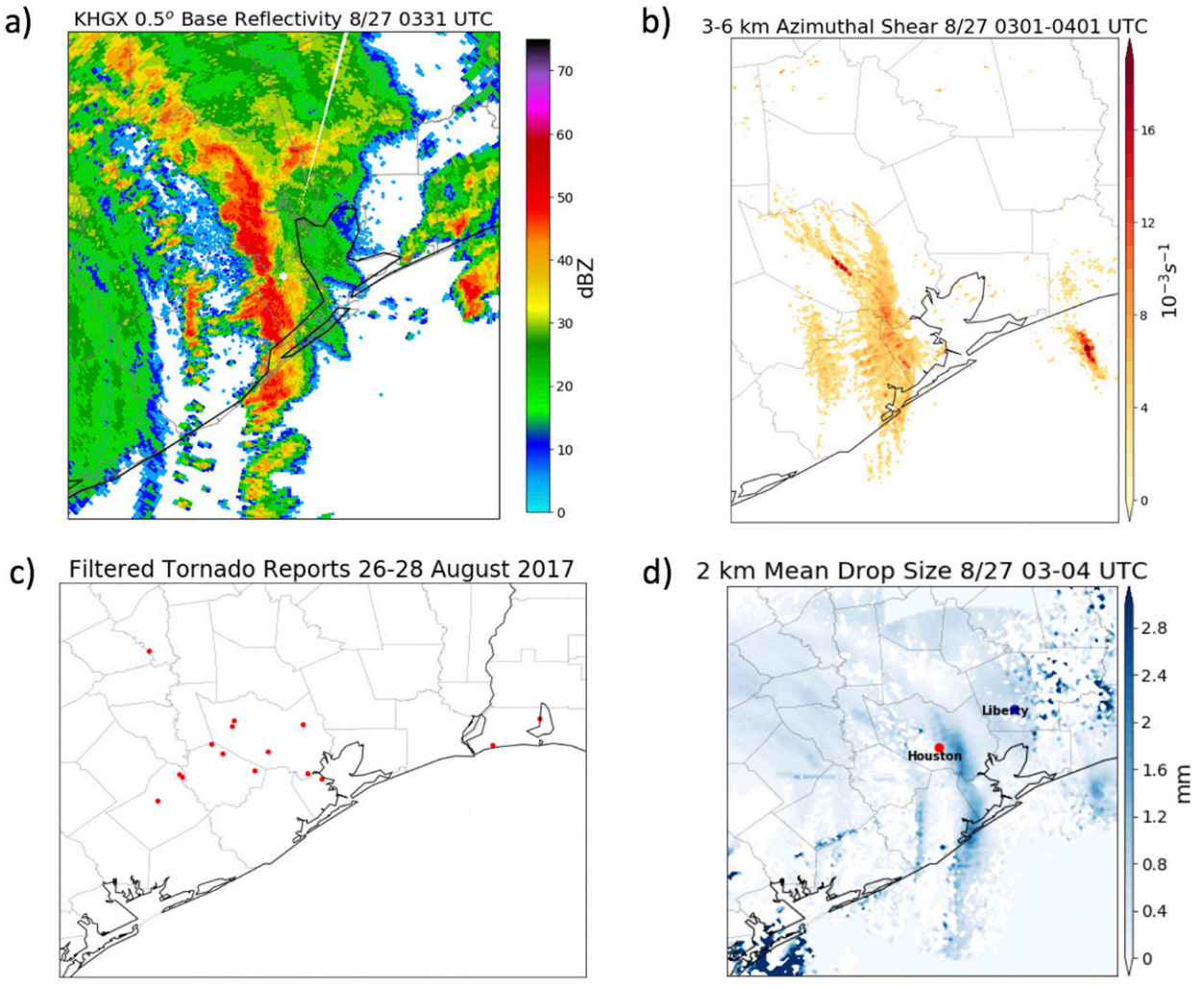

FIG. 15. (a) The 0.5° Z_H from the KHGX WSR-88D at 0331 UTC 27 Aug showing the line of training supercells east of Houston, (b) 3–6-km azimuthal shear, (c) SPC filtered tornado reports from 26 to 28 Aug, and (d) a Z_{DR}- and K_{DP}-weighted drop size estimation in tropical, convective rainfall (Gorgucci et al. 2002).

within the overall broad, excessive precipitation event that occurred over the region. While this study examines the specific case of Hurricane Harvey to quantify PE and incorporate polarimetric radar observations in landfalling tropical cyclones, a similar framework can be used for other landfalling tropical cyclones such as Irma, Florence, and Michael using the WSR-88D network. Similarly, this methodology can be expanded upon by looking at radar observations from the NASA Global Precipitation Measurements (GPM) Mission using the dual-frequency precipitation radar to provide an additional perspective of PE in tropical cyclones on a global scale using spaceborne remote sensing.

Acknowledgments. The authors thank Ryann Wakefield, Jordan Christian, Greg Jennrich, Addison Alford, Ryan Lagerquist, and Amanda Murphy for their constructive feedback, comments, and guidance towards this work. Additionally, the authors thank Travis Smith, Steven Martinaitis, Micheal Simpson, Heather Reeves, and Kiel Ortega at CIMMS and the NOAA National Severe Storms Laboratory for processing and providing the MRMS radar-derived rotation tracks and gauge-corrected precipitation data that were used in this study.

REFERENCES

Ashley, S. T., and W. S. Ashley, 2008: Flood fatalities in the United States. *J. Appl. Meteor. Climatol.*, **47**, 805–818, https://doi.org/10.1175/2007JAMC1611.1.

Austin, P. M., 1987: Relation between measured radar reflectivity and surface rainfall. *Mon. Wea. Rev.*, **115**, 1053–1070, https://doi.org/10.1175/1520-0493(1987)115<1053:RBMRRA>2.0.CO;2.

Bechini, R., L. Baldini, R. Cremonini, and E. Gorgucci, 2008: Differential reflectivity calibration for operational radars.

J. Atmos. Oceanic Technol., **25**, 1542–1555, https://doi.org/10.1175/2008JTECHA1037.1.

Blake, E. S., and D. A. Zelinsky, 2018: National Hurricane Center Tropical Cyclone Report: Hurricane Harvey (AL092017). NOAA/NWS, 77 pp., https://www.nhc.noaa.gov/data/tcr/AL092017_Harvey.pdf.

Bowman, K. P., and C. R. Homeyer, 2017: GridRad–Three-Dimensional Gridded NEXRAD WSR-88D Radar Data, version 3.1. National Center for Atmospheric Research, Computational and Information Systems Laboratory, accessed August 2019, https://doi.org/10.5065/D6NK3CR7.

Bringi, V. N., V. Chandrasekar, N. Balakrishnan, and D. S. Zrnić, 1990: An examination of propagation effects in rainfall on radar measurements at microwave frequencies. *J. Atmos. Oceanic Technol.*, **7**, 829–840, https://doi.org/10.1175/1520-0426(1990)007<0829:AEOPEI>2.0.CO;2.

Brown, B. R., M. M. Bell, and A. J. Frambach, 2016: Validation of simulated hurricane drop size distributions using polarimetric radar. *Geophys. Res. Lett.*, **43**, 910–917, https://doi.org/10.1002/2015GL067278.

Browning, K., 1977: The structure and mechanism of hailstorms. *Hail: A Review of Hail Science and Hail Suppression*, *Meteor. Monogr.*, No. 16, Amer. Meteor. Soc., 1–43.

Carr, N., P. E. Kirstetter, J. J. Gourley, and Y. Hong, 2017: Polarimetric signatures of midlatitude warm-rain precipitation events. *J. Appl. Meteor. Climatol.*, **56**, 697–711, https://doi.org/10.1175/JAMC-D-16-0164.1.

Chappell, C. F, 1986: Quasi-stationary convective events. *Mesoscale Meteorology and Forecasting*, P. S. Ray, Ed., Amer. Meteor. Soc., 289–310.

Cifelli, R., V. Chandrasekar, S. Lim, P. C. Kennedy, Y. Wang, and S. A. Rutledge, 2011: A new dual-polarization radar rainfall algorithm: Application in Colorado precipitation events. *J. Atmos. Oceanic Technol.*, **28**, 352–364, https://doi.org/10.1175/2010JTECHA1488.1.

Crosson, W. L., C. E. Duchon, R. Raghavan, and S. J. Goodman, 1996: Assessment of rainfall estimates using a standard Z–R relationship and the probability matching method applied to composite radar data in central Florida. *J. Appl. Meteor.*, **35**, 1203–1219, https://doi.org/10.1175/1520-0450(1996)035<1203:AOREUA>2.0.CO;2.

Crum, T. D., and R. L. Alberty, 1993: The WSR-88D and the WSR-88D operational support facility. *Bull. Amer. Meteor. Soc.*, **74**, 1669–1687, https://doi.org/10.1175/1520-0477(1993)074<1669:TWATWO>2.0.CO;2.

Daly, C., R. P. Neilson, and D. L. Phillips, 1994: A statistical-topographic model for mapping climatological precipitation over mountainous terrain. *J. Appl. Meteor.*, **33**, 140–158, https://doi.org/10.1175/1520-0450(1994)033<0140:ASTMFM>2.0.CO;2.

Davis, R. S., 2001: Flash flood forecast and detection methods. *Severe Convective Storms*, Meteor. Monogr., No. 50, Amer. Meteor. Soc., 481–526, https://doi.org/10.1175/0065-9401-28.50.481.

Didlake, A. C., and M. R. Kumjian, 2017: Examining polarimetric radar observations of bulk microphysical structures and their relation to Vortex Kinematics in Hurricane Arthur (2014). *Mon. Wea. Rev.*, **145**, 4521–4541, https://doi.org/10.1175/MWR-D-17-0035.1.

Didlake, A. C., Jr., and M. R. Kumjian, 2018: Examining storm asymmetries in Hurricane Irma (2017) using polarimetric radar observations. *Geophys. Res. Lett.*, **45**, 13 513–13 522, https://doi.org/10.1029/2018GL080739.

Doswell, C. A., H. E. Brooks, and R. A. Maddox, 1996: Flash flood forecasting: An ingredients-based methodology. *Wea. Forecasting*, **11**, 560–581, https://doi.org/10.1175/1520-0434(1996)011<0560:FFFAIB>2.0.CO;2.

Duda, J. D., and W. A. Gallus, 2010: Spring and summer midwestern severe weather reports in supercells compared to other morphologies. *Wea. Forecasting*, **25**, 190–206, https://doi.org/10.1175/2009WAF2222338.1.

Edwards, R., 2012: Tropical cyclone tornadoes: A review of knowledge in research and prediction. *Electron. J. Severe Storms Meteor.*, **7** (6), 1–61, https://ejssm.org/ojs/index.php/ejssm/article/viewArticle/97.

——, S. Overpeck, G. R. Woodall, and C. J. Nowotarski, 2018: Tornadoes in Hurricane Harvey: Documentation and environmental analysis. *Proc. 29th Conf. Severe Local Storms*, Stowe, VT, Amer. Meteor. Soc., P52, https://ams.confex.com/ams/29SLS/webprogram/Paper348127.html.

Foote, G. B., and J. C. Fankhauser, 1973: Airflow and moisture budget beneath a Northeast Colorado Hailstorm. *J. Appl. Meteor.*, **12**, 1330–1353, https://doi.org/10.1175/1520-0450(1973)012<1330:AAMBBA>2.0.CO;2.

Giangrande, S. E., and A. V. Ryzhkov, 2008: Estimation of rainfall based on the results of polarimetric echo classification. *J. Appl. Meteor. Climatol.*, **47**, 2445–2462, https://doi.org/10.1175/2008JAMC1753.1.

Gorgucci, E., G. Scarchilli, and V. Chandrasekar, 1992: Calibration of radars using polarimetric techniques. *IEEE Trans. Geosci. Remote Sens.*, **30**, 853–858, https://doi.org/10.1109/36.175319.

——, V. Chandrasekar, V. N. Bringi, and G. Scarchilli, 2002: Estimation of raindrop size distribution parameters from polarimetric radar measurements. *J. Atmos. Sci.*, **59**, 2373–2384, https://doi.org/10.1175/1520-0469(2002)059<2373:EORSDP>2.0.CO;2.

Griffin, E. M., T. J. Schuur, D. R. MacGorman, M. R. Kumjian, and A. O. Fierro, 2014: An electrical and polarimetric analysis of the overland reintensification of tropical storm erin (2007). *Mon. Wea. Rev.*, **142**, 2321–2344, https://doi.org/10.1175/MWR-D-13-00360.1.

Herzegh, P. H., and A. R. Jameson, 1992: Observing precipitation through dual-polarization radar measurements. *Bull. Amer. Meteor. Soc.*, **73**, 1365–1374, https://doi.org/10.1175/1520-0477(1992)073<1365:OPTDPR>2.0.CO;2.

Hisham Mohd Anip, M., and P. Market, 2007: Dominant factors influencing precipitation efficiency in a continental midlatitude location. *Tellus*, **59A**, 122–126, https://doi.org/10.1111/J.1600-0870.2006.00208.X.

Hitchens, N., and H. Brooks, 2013: Preliminary investigation of the contribution of supercell thunderstorms to the climatology of heavy and extreme precipitation in the United States. *Atmos. Res.*, **123**, 206–210, https://doi.org/10.1016/J.ATMOSRES.2012.06.023.

Homeyer, C. R., and M. R. Kumjian, 2015: Microphysical characteristics of overshooting convection from polarimetric radar observations. *J. Atmos. Sci.*, **72**, 870–891, https://doi.org/10.1175/JAS-D-13-0388.1.

Houze, R. A., 1997: Stratiform precipitation in regions of convection: A meteorological paradox? *Bull. Amer. Meteor. Soc.*, **78**, 2179–2196, https://doi.org/10.1175/1520-0477(1997)078<2179:SPIROC>2.0.CO;2.

Jessup, S. M., and A. T. DeGaetano, 2008: A statistical comparison of the properties of flash flooding and non-flooding precipitation events in portions of New York and Pennsylvania. *Wea. Forecasting*, **23**, 114–130, https://doi.org/10.1175/2007WAF2006066.1.

Kumjian, M., 2012: The impact of precipitation physical processes on the polarimetric radar variables. Ph.D. dissertation, University of Oklahoma, 327 pp.

——, 2013a: Principles and applications of dual-polarization weather radar. Part I: Description of the polarimetric radar variables. *J. Oper. Meteor.*, **1**, 226–242, https://doi.org/10.15191/nwajom.2013.0119.

——, 2013b: Principles and applications of dual-polarization weather radar. Part II: Warm- and cold-season applications. *J. Oper. Meteor.*, **1**, 243–264, https://doi.org/10.15191/nwajom.2013.0120.

——, 2013c: Principles and applications of dual-polarization weather radar. Part III: Artifacts. *J. Oper. Meteor.*, **1**, 265–274, https://doi.org/10.15191/nwajom.2013.0121.

——, A. P. Khain, N. Benmoshe, E. Ilotoviz, A. V. Ryzhkov, and V. T. J. Phillips, 2014: The anatomy and physics of zdr columns: Investigating a polarimetric radar signature with a spectral bin microphysical model. *J. Appl. Meteor. Climatol.*, **53**, 1820–1843, https://doi.org/10.1175/JAMC-D-13-0354.1.

Loney, M. L., D. S. Zrnić, J. M. Straka, and A. V. Ryzhkov, 2002: Enhanced polarimetric radar signatures above the melting level in a supercell storm. *J. Appl. Meteor.*, **41**, 1179–1194, https://doi.org/10.1175/1520-0450(2002)041<1179:EPRSAT>2.0.CO;2.

Markowski, P., and Y. Richardson, 2010: *Mesoscale Meteorology in Midlatitudes*. John Wiley and Sons, 430 pp.

Marwitz, J., 1972: Precipitation efficiency of thunderstorms on the high plains. *J. Rech. Atmos.*, **6**, 367–370.

May, R., S. Arms, P. Marsh, E. Bruning, and J. Leeman, 2017: Metpy: A Python package for meteorological data. Unidata, https://github.com/Unidata/MetPy.

McCaul, E. W., 1991: Buoyancy and shear characteristics of hurricane-tornado environments. *Mon. Wea. Rev.*, **119**, 1954–1978, https://doi.org/10.1175/1520-0493(1991)119<1954:BASCOH>2.0.CO;2.

McFarquhar, G. M., and R. List, 1991: The raindrop mean free path and collision rate dependence on rainrate for three-peak equilibrium and Marshall–Palmer distributions. *J. Atmos. Sci.*, **48**, 1999–2003, https://doi.org/10.1175/1520-0469(1991)048<1999:TRMFPA>2.0.CO;2.

Medlin, J. M., S. K. Kimball, and K. G. Blackwell, 2007: Radar and rain gauge analysis of the extreme rainfall during Hurricane Danny's (1997) landfall. *Mon. Wea. Rev.*, **135**, 1869–1888, https://doi.org/10.1175/MWR3368.1.

Mesinger, F., and Coauthors, 2006: North American Regional Reanalysis. *Bull. Amer. Meteor. Soc.*, **87**, 343–360, https://doi.org/10.1175/BAMS-87-3-343.

National Weather Service, 2001: Tropical Storm Allison: Heavy rains and floods, Texas and Louisiana, June 2001. National Weather Service, 37 pp., https://www.weather.gov/media/publications/assessments/allison.pdf.

——, 2018: Service assessment: August/September 2017 Hurricane Harvey. National Weather Service, 78 pp., https://www.weather.gov/media/publications/assessments/harvey6-18.pdf.

Newton, C. W., 1966: Circulations in large sheared cumulonimbus. *Tellus*, **18A**, 699–713, https://doi.org/10.1111/j.2153-3490.1966.tb00291.x.

Nielsen, E. R., and R. S. Schumacher, 2018: Dynamical insights into extreme short-term precipitation associated with supercells and mesovortices. *J. Atmos. Sci.*, **75**, 2983–3009, https://doi.org/10.1175/JAS-D-17-0385.1.

——, and ——, 2020a: Observations of extreme short-term precipitation associated with supercells and mesovortices. *Mon. Wea. Rev.*, **148**, 159–182, https://doi.org/10.1175/MWR-D-19-0146.1.

——, and ——, 2020b: Dynamical mechanisms supporting extreme rainfall accumulations in the Houston "Tax Day" 2016 flood. *Mon. Wea. Rev.*, **148**, 83–109, https://doi.org/10.1175/MWR-D-19-0206.1.

Radar Operations Center, 1991: NOAA Next Generation Radar (NEXRAD) Level 2 Base Data. NOAA National Centers for Environmental Information, accessed August 2019, https://doi.org/10.7289/V5W9574V.

Rappaport, E. N., 2000: Loss of life in the United States associated with recent Atlantic tropical cyclones. *Bull. Amer. Meteor. Soc.*, **81**, 2065–2073, https://doi.org/10.1175/1520-0477(2000)081<2065:LOLITU>2.3.CO;2.

——, 2014: Fatalities in the United States from Atlantic tropical cyclones: New data and interpretation. *Bull. Amer. Meteor. Soc.*, **95**, 341–346, https://doi.org/10.1175/BAMS-D-12-00074.1.

——, and J. J. Fernandez-Partagas, 1997: History of the deadliest Atlantic tropical cyclones since the discovery of the New World. *Hurricanes*, H. F. Diaz and R. S. Pulwarty, Springer, 93–108, https://doi.org/10.1007/978-3-642-60672-4_5.

Reynolds, R. W., N. A. Rayner, T. M. Smith, D. C. Stokes, and W. Wang, 2002: An improved in situ and satellite sst analysis for climate. *J. Climate*, **15**, 1609–1625, https://doi.org/10.1175/1520-0442(2002)015<1609:AIISAS>2.0.CO;2.

Rosenfeld, D., D. B. Wolff, and D. Atlas, 1993: General probability-matched relations between radar reflectivity and rain rate. *J. Appl. Meteor.*, **32**, 50–72, https://doi.org/10.1175/1520-0450(1993)032<0050:GPMRBR>2.0.CO;2.

Ryzhkov, A. V., 2007: The impact of beam broadening on the quality of radar polarimetric data. *J. Atmos. Oceanic Technol.*, **24**, 729–744, https://doi.org/10.1175/JTECH2003.1.

——, S. E. Giangrande, and T. J. Schuur, 2005a: Rainfall estimation with a polarimetric prototype of WSR-88D. *J. Appl. Meteor.*, **44**, 502–515, https://doi.org/10.1175/JAM2213.1.

——, T. J. Schuur, D. W. Burgess, P. L. Heinselman, S. E. Giangrande, and D. S. Zrnić, 2005b: The joint polarization experiment: Polarimetric rainfall measurements and hydrometeor classification. *Bull. Amer. Meteor. Soc.*, **86**, 809–824, https://doi.org/10.1175/BAMS-86-6-809.

——, P. Zhang, H. Reeves, M. Kumjian, T. Tschallener, S. Trömel, and C. Simmer, 2016: Quasi-vertical profiles—A new way to look at polarimetric radar data. *J. Atmos. Oceanic Technol.*, **33**, 551–562, https://doi.org/10.1175/JTECH-D-15-0020.1.

SAIC, BOM, NHC, JTWC, and RDA, 1993: Global tropical cyclone "best track" position and intensity data. National Center for Atmospheric Research, Computational and Information Systems Laboratory, accessed November 2018, http://rda.ucar.edu/datasets/ds824.1/.

Schroeder, A., J. Basara, J. M. Shepherd, and S. Nelson, 2016: Insights into atmospheric contributors to urban flash flooding across the United States using an analysis of rawinsonde data and associated calculated parameters. *J. Appl. Meteor. Climatol.*, **55**, 313–323, https://doi.org/10.1175/JAMC-D-14-0232.1.

Seliga, T. A., and V. N. Bringi, 1976: Potential use of radar differential reflectivity measurements at orthogonal polarizations for measuring precipitation. *J. Appl. Meteor.*, **15**, 69–76, https://doi.org/10.1175/1520-0450(1976)015<0069:PUORDR>2.0.CO;2.

Smith, J. A., M. L. Baeck, Y. Zhang, and C. A. Doswell, 2001: Extreme rainfall and flooding from supercell thunderstorms. *J. Hydrometeor.*, **2**, 469–489, https://doi.org/10.1175/1525-7541(2001)002<0469:ERAFFS>2.0.CO;2.

Smith, T. M., and K. Elmore, 2004: The use of radial velocity derivatives to diagnose rotation and divergence. *11th Conf. on Aviation, Range, and Aerospace*, Hyannis, MA, Amer. Meteor. Soc., P5.6, https://ams.confex.com/ams/11aram22sls/techprogram/paper_81827.htm.

——, and Coauthors, 2016: Multi-Radar Multi-Sensor (MRMS) severe weather and aviation products: Initial operating capabilities. *Bull. Amer. Meteor. Soc.*, **97**, 1617–1630, https://doi.org/10.1175/BAMS-D-14-00173.1.

Squires, P., 1956: The micro-structure of cumuli in maritime and continental air. *Tellus*, **8A**, 443–444, https://doi.org/10.1111/j.2153-3490.1956.tb01246.x.

Testud, J., E. Le Bouar, E. Obligis, and M. Ali-Mehenni, 2000: The rain profiling algorithm applied to polarimetric weather radar. *J. Atmos. Oceanic Technol.*, **17**, 332–356, https://doi.org/10.1175/1520-0426(2000)017<0332:TRPAAT>2.0.CO;2.

Ulbrich, C. W., and D. Atlas, 2008: Radar measurement of rainfall with and without polarimetry. *J. Appl. Meteor. Climatol.*, **47**, 1929–1939, https://doi.org/10.1175/2007JAMC1804.1.

van Lier-Walqui, M., and Coauthors, 2016: On polarimetric radar signatures of deep convection for model evaluation: Columns of specific differential phase observed during MC3E. *Mon. Wea. Rev.*, **144**, 737–758, https://doi.org/10.1175/MWR-D-15-0100.1.

Vitale, J., and T. Ryan, 2013: Operational recognition of high precipitation efficiency and low-echo-centroid convection. *J. Oper. Meteor.*, **1**, 128–143, https://doi.org/10.15191/nwajom.2013.0112.

Weisman, M. L., and J. B. Klemp, 1984: The structure and classification of numerically simulated convective storms in directionally varying wind shears. *Mon. Wea. Rev.*, **112**, 2479–2498, https://doi.org/10.1175/1520-0493(1984)112<2479:TSACON>2.0.CO;2.

Ye, H., E. J. Fetzer, S. Wong, A. Behrangi, E. T. Olsen, J. Cohen, B. H. Lambrigtsen, and L. Chen, 2014: Impact of increased water vapor on precipitation efficiency over northern Eurasia. *Geophys. Res. Lett.*, **41**, 2941–2947, https://doi.org/10.1002/2014GL059830.

Zhang, J., and Coauthors, 2011: National Mosaic and Multi-Sensor QPE (NMQ) system: Description, results, and future plans. *Bull. Amer. Meteor. Soc.*, **92**, 1321–1338, https://doi.org/10.1175/2011BAMS-D-11-00047.1.

Zhang, Y., L. Liu, H. Wen, C. Wu, and Y. Zhang, 2018: Evaluation of the polarimetric-radar quantitative precipitation estimates of an extremely heavy rainfall event and nine common rainfall events in Guangzhou. *Atmosphere*, **9**, 330, https://doi.org/10.3390/atmos9090330.

Zrnić, D. S., and A. Ryzhkov, 1996: Advantages of rain measurements using specific differential phase. *J. Atmos. Oceanic Technol.*, **13**, 454–464, https://doi.org/10.1175/1520-0426(1996)013<0454:AORMUS>2.0.CO;2.

——, and A. V. Ryzhkov, 1999: Polarimetry for weather surveillance radars. *Bull. Amer. Meteor. Soc.*, **80**, 389–406, https://doi.org/10.1175/1520-0477(1999)080<0389:PFWSR>2.0.CO;2.